U.S. ARMY
NASA
ARL
RESEARCH LABORATORY

Aerodynamic Design Study of Advanced Multistage Axial Compressor

Louis M. Larosiliere
U.S. Army Research Laboratory, Glenn Research Center, Cleveland, Ohio

Jerry R. Wood
Glenn Research Center, Cleveland, Ohio

Michael D. Hathaway
U.S. Army Research Laboratory, Glenn Research Center, Cleveland, Ohio

Adam J. Medd and Thong Q. Dang
Syracuse University, Syracuse, New York

20031003 110

Since its founding, NASA has been dedicated to the advancement of aeronautics and space science. The NASA Scientific and Technical Information (STI) Program Office plays a key part in helping NASA maintain this important role.

The NASA STI Program Office is operated by Langley Research Center, the Lead Center for NASA's scientific and technical information. The NASA STI Program Office provides access to the NASA STI Database, the largest collection of aeronautical and space science STI in the world. The Program Office is also NASA's institutional mechanism for disseminating the results of its research and development activities. These results are published by NASA in the NASA STI Report Series, which includes the following report types:

- TECHNICAL PUBLICATION. Reports of completed research or a major significant phase of research that present the results of NASA programs and include extensive data or theoretical analysis. Includes compilations of significant scientific and technical data and information deemed to be of continuing reference value. NASA's counterpart of peer-reviewed formal professional papers but has less stringent limitations on manuscript length and extent of graphic presentations.

- TECHNICAL MEMORANDUM. Scientific and technical findings that are preliminary or of specialized interest, e.g., quick release reports, working papers, and bibliographies that contain minimal annotation. Does not contain extensive analysis.

- CONTRACTOR REPORT. Scientific and technical findings by NASA-sponsored contractors and grantees.

- CONFERENCE PUBLICATION. Collected papers from scientific and technical conferences, symposia, seminars, or other meetings sponsored or cosponsored by NASA.

- SPECIAL PUBLICATION. Scientific, technical, or historical information from NASA programs, projects, and missions, often concerned with subjects having substantial public interest.

- TECHNICAL TRANSLATION. English-language translations of foreign scientific and technical material pertinent to NASA's mission.

Specialized services that complement the STI Program Office's diverse offerings include creating custom thesauri, building customized databases, organizing and publishing research results . . . even providing videos.

For more information about the NASA STI Program Office, see the following:

- Access the NASA STI Program Home Page at *http://www.sti.nasa.gov*

- E-mail your question via the Internet to help@sti.nasa.gov

- Fax your question to the NASA Access Help Desk at 301–621–0134

- Telephone the NASA Access Help Desk at 301–621–0390

- Write to:
  NASA Access Help Desk
  NASA Center for AeroSpace Information
  7121 Standard Drive
  Hanover, MD 21076

NASA/TP—2002-211568

ARL-TR-2859

Aerodynamic Design Study of Advanced Multistage Axial Compressor

Louis M. Larosiliere
U.S. Army Research Laboratory, Glenn Research Center, Cleveland, Ohio

Jerry R. Wood
Glenn Research Center, Cleveland, Ohio

Michael D. Hathaway
U.S. Army Research Laboratory, Glenn Research Center, Cleveland, Ohio

Adam J. Medd and Thong Q. Dang
Syracuse University, Syracuse, New York

National Aeronautics and
Space Administration

Glenn Research Center

December 2002

Aerodynamic Design Study of Advanced Multistage Axial Compressor

Louis M. Larosiliere
U.S. Army Research Laboratory
Glenn Research Center
Cleveland, Ohio 44135

Jerry R. Wood
National Aeronautics and Space Administration
Glenn Research Center
Cleveland, Ohio 44135

Michael D. Hathaway
U.S. Army Research Laboratory
Glenn Research Center
Cleveland, Ohio 44135

Adam J. Medd and Thong Q. Dang
Syracuse University
Syracuse, New York 13244

Summary

As a direct response to the need for further performance gains from current multistage axial compressors, an investigation of advanced aerodynamic design concepts that will lead to compact, high-efficiency, and wide-operability configurations is being pursued. Part I of this report describes the projected level of technical advancement relative to the state of the art and quantifies it in terms of basic aerodynamic technology elements of current design systems. A rational enhancement of these elements is shown to lead to a substantial expansion of the design and operability space. Aerodynamic design considerations for a four-stage core compressor intended to serve as a vehicle to develop, integrate, and demonstrate aerotechnology advancements are discussed. This design is biased toward high efficiency at high loading. Three-dimensional blading and spanwise tailoring of vector diagrams guided by computational fluid dynamics (CFD) are used to manage the aerodynamics of the high-loaded endwall regions. Certain deleterious flow features, such as leakage-vortex-dominated endwall flow and strong shock-boundary-layer interactions, were identified and targeted for improvement. However, the preliminary results were encouraging and the front two stages were extracted for further aerodynamic trimming using a three-dimensional inverse design method described in part II of this report.

The benefits of the inverse design method are illustrated by developing an appropriate pressure-loading strategy for transonic blading and applying it to reblade the rotors in the front two stages of the four-stage configuration. Multistage CFD simulations based on the average passage formulation indicated an overall efficiency potential far exceeding current practice for the front two stages. Results of the CFD simulation at the aerodynamic design point are interrogated to identify areas requiring additional development. In spite of the significantly higher aerodynamic loadings, advanced CFD-based tools were able to effectively guide the design of a very efficient axial compressor under state-of-the-art aeromechanical constraints.

Introduction

The intensely competitive aeropropulsion sector places some of the most stringent requirements on turbo-compressors. A common challenge is aerothermodynamic optimization subject to conflicting economic

and system constraints, such as reduced cost, low environmental emissions, and wide operability under adverse conditions. An interesting account of the first 50 years of aeropropulsion gas turbines was offered by Singh (ref. 1), who clarified the trail taken to improve fuel economy by way of higher thermal and propulsive efficiencies. Figure 1 shows the effects of component efficiency, compressor delivery temperature, and turbine entry temperature on the thermal efficiency of a simple Brayton cycle using a hydrocarbon fuel and metallic materials. The implication is that overall polytropic efficiencies of 94 percent with compression ratios in the range of 60:1 and beyond must be realized to arrive at thermal efficiencies surpassing 55 percent. Techniques for achieving low losses at high aerodynamic loadings have therefore received renewed interest in many recent turbomachinery studies (refs. 2 and 3).

Turbocompression technology has been advanced continuously by higher work capacity per stage as a result of increases in rotor speed, aerodynamic loading, and throughflow Mach numbers. Using sophisticated diagnostic tools involving CFD and measurement techniques, more suitable blade shapes with relatively low losses at higher diffusion and Mach number levels have been deployed. Better materials and matured structural analysis methods have also allowed increases in rotor speed with significant weight reductions. Improved mechanical design and fabrication techniques have raised the quality of current products.

The quest for further aerodynamic performance advancements is becoming progressively more difficult because of a dwindling residue of losses. Prohibitive demands such as performance invariance to various operating conditions and hardware degradation are imposing severe aerodynamic limitations. Easing these limitations requires the application of new technology to manage the particular flow structures responsible for performance shortfalls. Effective strategies for achieving this are not at all clear. A vital issue is whether to advance by refining and extending well-proven concepts, perhaps in the face of diminishing returns, or by changing to something more unpredictable yet inviting.

A research program being conducted at the Glenn Research Center is investigating advanced design concepts that will lead to compact, high-efficiency, and wide-operability compressors. This is a direct response to the need for further performance gains from current turbomachinery systems. To service these gains, a combination of evolutionary and revolutionary approaches to technology development was selected. The evolutionary approach employs advancements in simulation techniques to refine traditional design concepts in a bid for higher efficiencies at increased aerodynamic loading levels, whereas the revolutionary approach attempts to explore unconventional concepts and paradigms for increased pressure ratio, higher efficiencies, and wider operability.
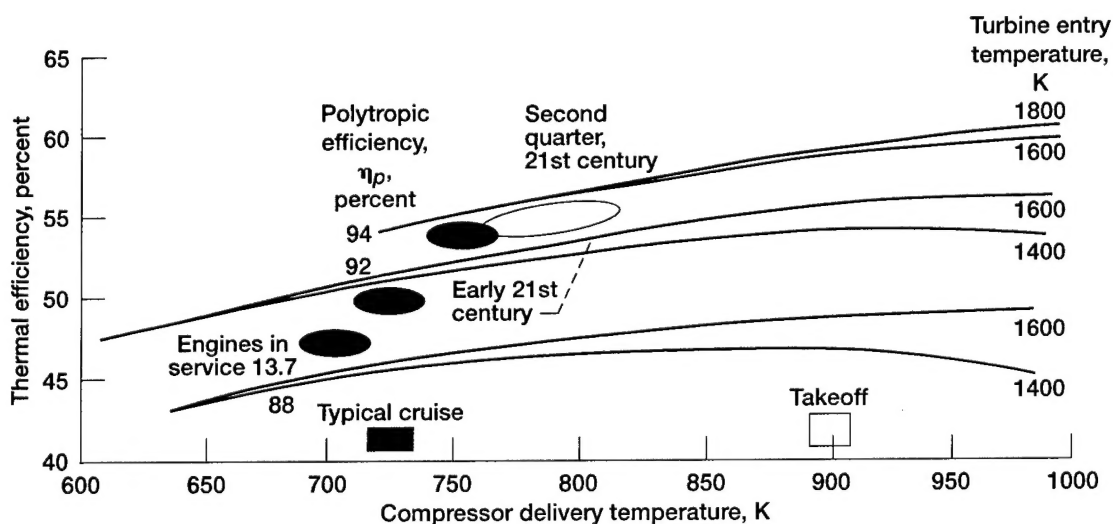

Figure 1.—Impact of component efficiency on thermal efficiency (Singh, ref. 1)

Part I of this report depicts the level of technical advancement being sought, quantifies this advancement in terms of the basic aerodynamic technology elements of current design systems, and identifies a four-stage core compressor configuration for advanced technology development. A preliminary aerodynamic design of the four-stage configuration is described in the context of current practice. Custom-tailored blade contours were initially developed from mean camber surfaces derived from axisymmetric stream surfaces generated by an inverse throughflow calculation. Isolated blade-row CFD simulations provided some guidance to fine-tune the blading. A multistage CFD computation using a mixing plane scheme indicated an efficiency potential for the four-stage compressor that is within current standards. In addition, performance-limiting flow features, such as leakage-vortex-dominated endwall action and/or reaction and strong shock-boundary-layer interactions, were identified and targeted for improvement. The possibility of further performance gains requires a design method that effectively extends the custom-tailored blading philosophy into the endwall regions and adequately allows matching of blade rows in the multistage environment.

In part II of the report, an aerodynamic design of the front two stages of the four-stage configuration is developed using the best available CFD tools. The three-dimensional inverse design method of Dang (ref. 4) was used to define advanced transonic rotor blading. To illustrate the benefits of this method, the front two stages of the four-stage configuration were rebladed and the performance potential evaluated. The multistage aerodynamic environment was modeled using the substantiated method of Adamczyk (ref. 5). This modeling permitted a reliable prediction of the performance potential of the two-stage group and guided design revisions, including the facilitation of stage matching. The results show the critical role of this method and illustrate achievable performance using an evolutionary approach buttressed by advanced turbomachinery CFD.

Geometric information for all blade rows is given in appendix A, and spanwise profiles of axisymmetric averaged flow properties extracted from the multistage CFD simulation of the front two-stages at the aerodynamic design point are given in appendix B.

Symbols

A_{ex}	passage exit area, in.
A_θ	tangential projection of blade surface area
D_{factor}	diffusion factor
E	effectivity ratio
f	blade mean camber surface, $f(r,z)$
f_{stack}	blade stacking line, $f_{stack}(r)$
ΔH	total enthalpy change, BTU/lbm
L_{diff}	equivalent diffusion length
$L_{diff}/\sqrt{A_{ex}}$	ratio of equivalent diffusion length to effective passage exit width
M_1	inlet Mach number
$\dot{m}$	mass flow rate, lbm/s
P	total pressure, psia
PR	pressure ratio
p	static pressure, psia
Δp	static-pressure difference between blade upper and lower surfaces at fixed axial positions, $\Delta p = \Delta p(r,z)$
Re_c	chord Reynolds number
T	blade thickness distribution, $T(r,z)$
t/g	ratio of clearance to staggered spacing
U	blade speed, ft/s
V	velocity, ft/s
$\overline{V}_\theta$	absolute tangential velocity, ft/s
Wc	inlet corrected flow, lbm/s
z/s	ratio of axial spacing to pitch
α	swirl angle from axial direction, deg
η	efficiency, percent

Λ	blade aspect ratio; ratio of average length to pitchline chord
σ	solidity; ratio of chord to average tangential spacing
φ	flow coefficient, V_z/U_m
ψ	work coefficient, $\Delta H/U_m^2$
Ω	corrected mechanical speed, rpm

Subscripts:

abs	absolute
ex	exit
in	inlet
le	leading edge
m	meanline
max	maximum
p	polytropic
ref	reference
rel	relative
t	total
te	trailing edge
tip	tip
tt	total to total
z	axial

Part I: Level of Technical Advancement

Basic Aerodynamic Technology Elements

Aerodynamic loading and loss synthesis.—Turbocompressor aerodynamics comprises a complex array of intimately linked thermofluid processes that are difficult to separate into neat compartments. However, simplified models, which sufficiently incorporate the important physical phenomena, have been synthesized into design systems. Three essential aerodynamic technology elements of such design systems are (1) entropy production or loss; (2) aerodynamic transport including spanwise mixing; and (3) aerodynamic stability. The demarcation of these three elements is sometimes distorted by various empirical correlations that implicitly account for aerodynamic transport. Denton (ref. 6) gives a good physical description of entropy production in turbomachines and Greitzer (ref. 7) does likewise for aerodynamic stability. Adamczyk (ref. 5) and Adkins and Smith (ref. 8) discuss aerodynamic transport phenomena in turbocompressors.

An adaptation of the loss model of Koch and Smith (ref. 9) and the stage maximum static-pressure-rise prediction method of Koch (ref. 10) was used to estimate both the efficiency potential and the maximum aerodynamic loading capability for the present study. The losses are grouped according to source: (1) viscous dissipation along the blade-surface profile and the resultant wake mixing; (2) endwall viscous shear including interactions with secondary and leakage flows; and (3) shocks on the blading. Blade-surface-profile losses are linked to suction-surface diffusion (V_{max}/V_{te}), blade trailing-edge thickness, Reynolds number, and surface roughness. Endwall losses that have been determined from hub and casing viscous layer measurements are related to aspect ratio, solidity, blade stagger, endwall clearance, blade-row axial spacing, and aerodynamic loading level. The shock loss model relates passage shock losses to inlet and exit Mach numbers. A leading-edge bow shock loss is calculated based on the inlet Mach number and leading-edge thickness.

The stage maximum static-pressure-rise potential is linked to stage geometric parameters (e.g., solidity, aspect ratio, stagger, etc.) by a correlation based on an analogy between compressor blade passages and straight diffusers. There are also corrections for Reynolds number, endwall leakage, and blade-row axial spacing. The blading is averaged over a stage without separating the rotor and stator performance. This is a simple yet effective method to complement conceptual design calculations made at a representative section of a machine (i.e., meanline with implicit accounting of aerotransport). A relative aerodynamic loading parameter is defined by the ratio of the actual stage pressure-rise coefficient to that predicted by the correlation (the effectivity ratio E). Hence, an effectivity of 1 ($E=1.0$) indicates limit loading. It can be argued that this is a more appropriate indicator of aerodynamic loading from the point of view of instability initiated by the endwall flow. Measurements (ref. 11) have indicated that for well-designed blading with adequate circulation capacity, aerodynamic instability is likely to occur when endwall viscous layers increase to a limiting value dependent on effectivity and clearance.

The loss and aerodynamic loading models are unified in the sense that endwall loss and aerodynamic blockage are interrelated through aerodynamic loading. Thus, it is possible to determine the maximum pressure rise that can be obtained with moderate losses but not necessarily to determine the point of instability.

Anticipated technology advancements.—Changes to the loss and peak pressure-rise models were made to reflect anticipated aerodynamic technology advancements. It was surmised that low blade profile losses could be extended to higher diffusion levels by employing boundary-layer control techniques. Cascade tests and boundary-layer analysis have shown the potential for effecting this through diffusion control using tailored contours, staged diffusion (e.g., tandem and/or splittered architectures), or active diffusion control (e.g., surface transpiration or surface morphing). Figure 2 shows the postulated improvement in the ratio of the blade trailing-edge momentum thickness to the chord (i.e., viscous dissipation) relative to the state of the practice for a fixed-chord Reynolds number Re_c, an inlet Mach number M_1, and an axial velocity-density ratio (AVDR). Note that the reference is the state of the practice extracted from the method of Koch and Smith rather than state of the art because there are some uncertainties as to what the latter is. Also indicated is a data point assembled from measurements (ref. 12) on a compressor stator equipped with bleed slots for boundary-layer control. Research

currently underway should provide the knowledge required for practically achieving this control.

The stage maximum static-pressure-rise capability was postulated to increase relative to the state of the practice as shown in figure 3 for a fixed Reynolds number Re, the ratio of clearance to staggered spacing t/g, and the ratio of axial spacing to pitch z/s. The abscissa, $L_{diff}/\sqrt{A_{ex}}$, is the ratio of an equivalent diffusion length L_{diff} to an effective passage exit width (square root of passage exit area A_{ex}). This ratio can be expressed in terms of conceptual design parameters (solidity, aspect ratio, stagger) at a representative section of the machine. Shown on the ordinate is the stage maximum effective static-pressure-rise coefficient averaged over the rotor and stator (see ref. 10 for details). Also indicated in the figure is a data point from a low-speed rig with high-stagger, forward-swept blading. This data point is clearly above the state-of-the-practice level and reasons for this are under investigation using a simple physical model developed by Khalid et al. (ref. 13) for clearance-related blockage. The results from this model provide a quantification of aerodynamic blockage and a framework for screening endwall flow-management strategies based on casing treatment, vector diagrams, or pressure-loading distribution. The model corroborates the experiments of Lee and Greitzer (ref. 14), who demonstrated significant enhancements to the peak static-pressure rise of a blade row by the downstream removal of low-momentum flow and the
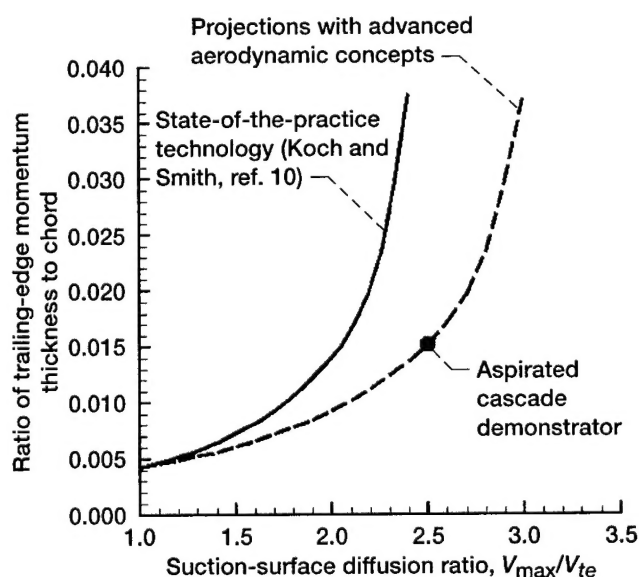

Figure 2.—Enhancements to profile loss model. Fixed-chord Reynolds number, Re_c, 10^6; inlet Mach number, M_1, 0.05; axial velocity-density ratio, AVDR, 1.0.
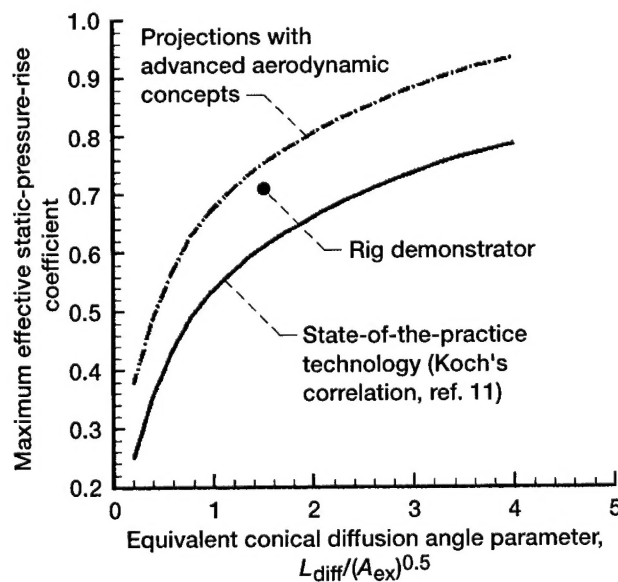

Figure 3.—Enhancements to stage maximum static-pressure rise. Fixed Reynolds number, Re, 130 000; ratio of clearance to staggered spacing, t/g, 0.055; ratio of axial spacing to pitch, z/s, 0.38.

upstream injection of flow with sufficient streamwise momentum.

It was judged that managing the endwall flow (e.g., secondary and leakage flow control) would also allow the blading to be more effective in that region, thereby reducing the required torque supplied to the rotor. This is accounted for in the endwall loss model by a 17-percent increase in the so-called tangential force thickness as described by Smith (ref. 11). All other loss sources, including direct shock losses, remained unmodified. The loss and aerodynamic loading models were integrated in a computerized preliminary design and analysis procedure, which allowed perturbations to specific aerodynamic technology elements to be readily appraised.

Extending the Design Envelope

The consequences of the aerodynamic advancements previously discussed were evaluated by comparing the design space of a prototypical stage with and without these advancements. A so-called Smith chart is used to represent the design and operational space of a turbocompressor stage with a given geometric form and flow type. This space is spanned by a suitably averaged flow coefficient ($\varphi = V_z/U_m$) and work coefficient ($\psi = \Delta H/U_m^2$). A relative aerodynamic loading parameter E (ψ, φ, geometric form, flow type) and an efficiency η (ψ, φ, geometric form, flow type) can be superimposed on this chart. It should be noted that the work coefficient is generally not a direct measure of aerodynamic loading as defined herein because it has no explicit link to mean static-pressure rise. This is reflected in the additional functional dependence of loading on flow coefficient and geometric form. The basic design challenge is to generate geometry that establishes a flow satisfying the ψ-φ requirements at high efficiency without exceeding the relative aerodynamic loading limit.

Geometric parameters for a prototypical single-stage axial compressor with a 21-in. maximum diameter were selected to illustrate the expanded design envelope and enhanced performance trends. A Smith chart for these parameters is shown in figure 4(a) using state-of-the-practice aerodynamic technology and in figure 4(b) with the postulated technology advancements. These plots are based on the following design choices: (1) zero swirl at stage inlet; (2) 60-percent-rotor-area contraction; (3) constant radius casing; and (4) axial velocity ratio of 1.0 across the stage. Since the rotor inlet specific flow (40.0 lbm/s-ft^2) is fixed, varying the flow coefficient
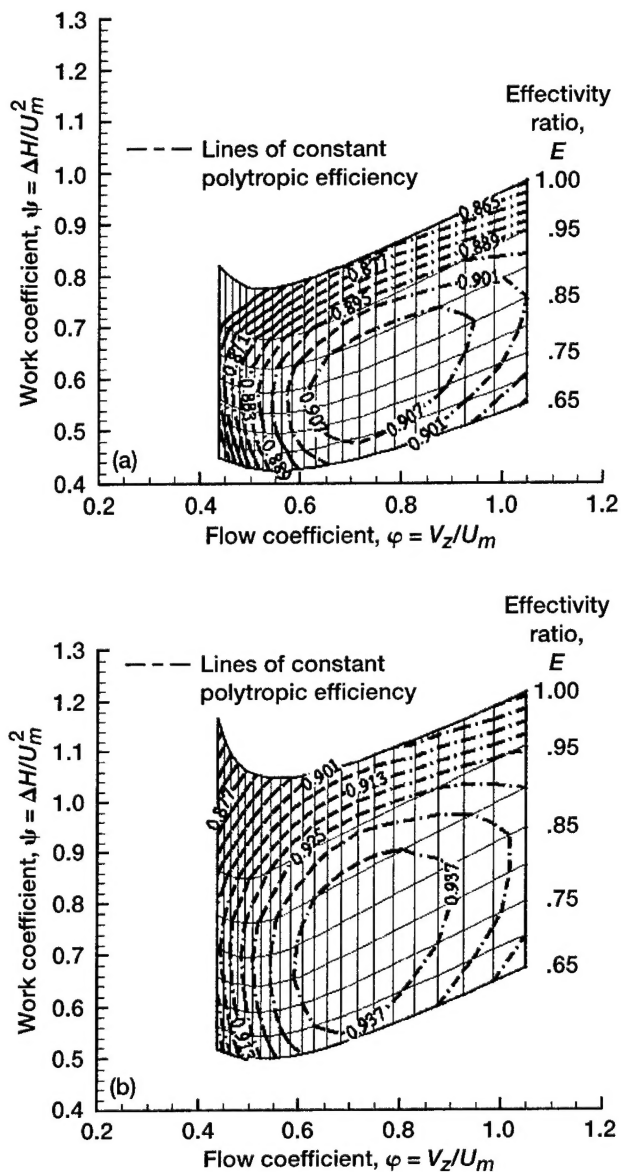

Figure 4.—Expanded design envelope and enhanced performance trends for prototypical single-stage axial compressor with 21-in. maximum diameter. Geometric parameters: rotor aspect ratio, 0.940; stator aspect ratio, 1.250; rotor solidity, 1.800; stator solidity, 1.700; Reynolds number, 3.26×10^6; ratio of clearance to staggered spacing, 0.0122. (a) Aerodynamic design space for state-of-the-practice technology. (b) Extended design envelope with advanced technology.

sweeps through both subsonic and transonic stages. In addition, fixing the inlet swirl and rotor area contraction generates a range of stage reactions as the flow coefficient is varied. The design point for individual stages of this particular type may be placed anywhere below the bound-
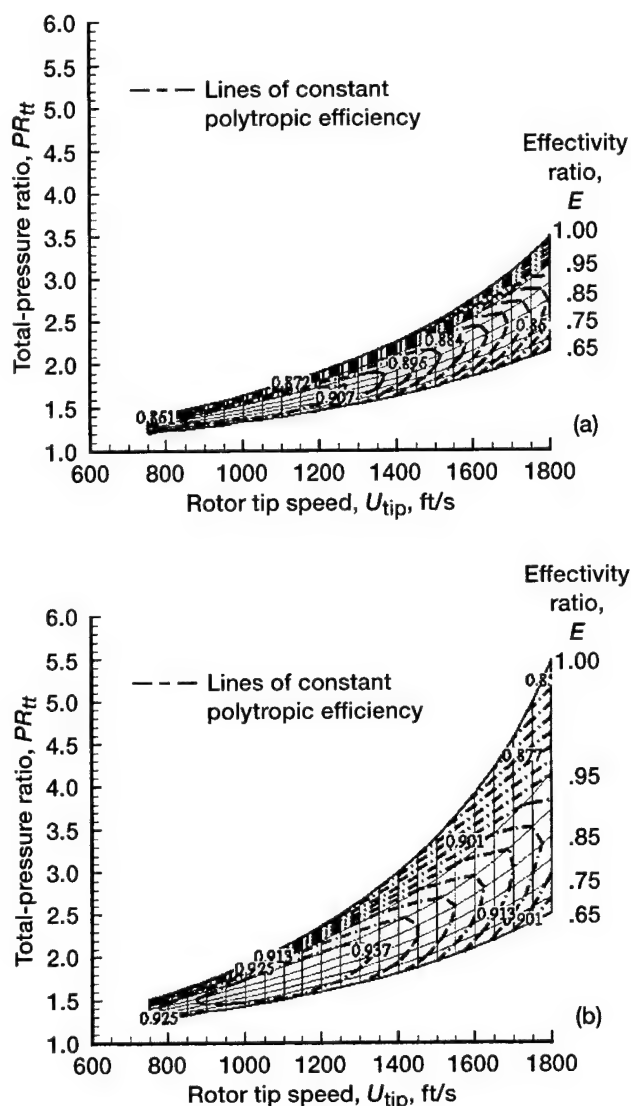
Figure 5.—Performance trends for prototypical stage. (a) State-of-the-practice technology. (b) Postulated advanced technology.

specific performance trends, figure 5 presents the effect of rotor tip speed and stage aerodynamic loading on stage total-pressure ratio and polytropic efficiency for the prototypical stage. Figure 5(a) is based on state-of-the-practice technology whereas figure 5(b) used the postulated aerodynamic technology advancements. The curves indicate that higher stage pressure ratios can be obtained by either increased tip speed or increased stage loading. Maximum dividends occur when both high loading and high tip speed are selected. The attainment of gains in pressure ratio is complicated by the need for high efficiency and wide operability. As loading is increased, losses tend to increase, and the potential for flow breakdown and aerodynamic instability is much greater. For the range of blade speeds shown in figure 5, the rotor tip relative Mach numbers vary from subsonic to high supersonic (i.e., greater than 1.6) values that can result in severe shock-related viscous losses.

For a fixed geometric envelope, the anticipated aerodynamic technology advancements suggest the potential for substantial expansion of the design space in the direction of higher work coefficients and stage total-pressure ratio. In addition, high efficiencies are extended to more elevated loadings. An increased pressure ratio per stage has traditionally been realized partly because of higher rotor speeds and primarily because of a lower aspect ratio, increased solidity, and higher stagger blading. These design choices, as can be inferred from figure 3, are often made to increase stage maximum static-pressure rise, thereby insuring adequate aerodynamic stability, which can often be accompanied by increased losses. A report by Wisler, Koch, and Smith (ref. 15) illustrates the interactions between different design choices and offers guidance for selecting multistage core compressor design parameters that have a high-efficiency potential. Based upon these results and some vector diagram considerations, figure 6 was constructed using information from actual compressor rig tests of machines having a certain degree of similarity in terms of tip clearance, stability requirement, specific flow, and blading. The abscissa is the Skoch parameter (SP), which is defined as

$$SP = \left[\frac{\sigma\varphi}{\Lambda\psi} \sqrt{1 + \left(\frac{1}{\varphi - \tan\alpha_{in}} \right)^2} \right]^{1/2}$$

where σ is the solidity (the ratio of chord to average tangential spacing); Λ is the blade aspect ratio (the ratio of average length to pitchline chord); and α_{in} is the stage
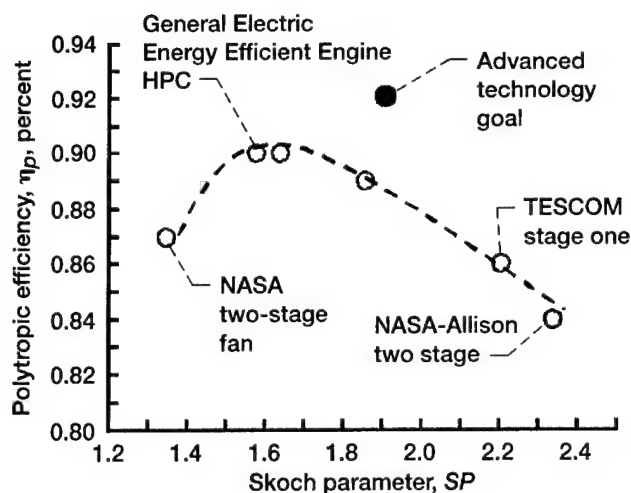
ary $E = 1.0$. For a given relative aerodynamic loading level E, flow and work coefficients can be selected to maximize efficiency.

Evident from figure 4 is a significant extension of the design space in the direction of higher work coefficients made possible by the postulated aerodynamic technology advancements. A potential increase of three points in peak polytropic efficiency is depicted along with the availability of more options for high-efficiency designs. Although the operability space, including flow range, is not directly addressed herein, the choice of how far and in which direction to extend the design space is greatly influenced by operability considerations. To illustrate

Figure 6.—Peak efficiency trends with various design choices for geometric form and vector diagram.

Figure 7.—Aerodynamic design system.

inlet swirl angle. This parameter, averaged over all stages, is analogous to a specific speed. The figure indicates the existence of judicious combinations of geometric form and vector diagram, which lead to high efficiencies. This is discussed by Wisler, Koch, and Smith, who showed the competition amongst various loss sources as aspect ratio and solidity are varied. Thus, the Skoch parameter provides a basis for trading geometric form and vector diagram (e.g., compactness and operability) to optimize efficiency.

To achieve the low parts count and high efficiency required of modern turbocompression systems, advanced technology concepts have been driven to high-work-coefficient and moderate-flow-coefficient designs. This trend is illustrated in figure 6 with the projected advanced technology goal for the chosen Skoch parameter. The advanced technology goal is a result of design choices orchestrated using the anticipated aerodynamic technology advancements. A discussion of these design choices follows.

Four-Stage, High-Pressure-Compressor Aerodynamic Technology Demonstrator

So far, no definitive path has been identified for achieving the assumed technology advancements. A research configuration was conceived with the intent of evaluating how far the use of advanced turbomachinery CFD and three-dimensional design concepts might permit one to progress in realizing high efficiency at increased loading levels. The objective was to configure a technology
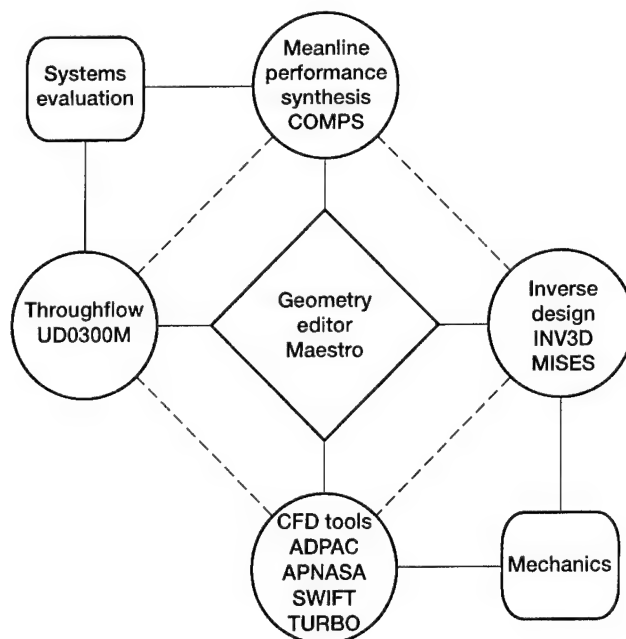
demonstrator compatible with current multistage core compressors for high-bypass-ratio turbofans. Although a specific application was not defined, a four-stage configuration under current aeromechanical constraints was selected. The execution of the aerodynamic design consists of an iterative loop between several computer programs as illustrated in figure 7. This methodology is essentially the same as that currently employed in most design offices with perhaps the exception of the three-dimensional inverse design method. The steps of the so-called preliminary design phase of this process and their interactions are outlined below; the more detailed design phase, including three-dimensional inverse design and multistage CFD, is described in part II.

Meanline performance synthesis.—Four parameters were established at the outset. The corrected specific flow (flow per unit annulus area) at the first rotor inlet was 40.0 lbm/s-ft^2 corresponding to an average axial inlet Mach number of 0.6, which is consistent with advanced core compressors. A maximum rotor corrected tip speed of 1500 ft/s was assumed based on turbine stress considerations for a high-bypass-ratio turbofan. An average Skoch parameter in the range of 1.5 to 2.0 was selected for high efficiency and compactness as suggested from figure 6. With a casing diameter of 21.08 in. and a radius ratio of 0.528 at the first rotor inlet, the mass flow corresponding to the prescribed specific flow was 70.0 lbm/s. The design can be scaled to different mass

TABLE I.—COMPARISON OF STAGE LOADING AND
POLYTROPIC EFFICIENCY

Stage	Cumulative total-pressure ratio, PR_{tt}	State of the practice		Advanced technology	
		Effectivity ratio, E	Polytropic efficiency, η_p, percent	Effectivity ratio, E	Polytropic efficiency, η_p, percent
1	2.372	0.894	0.890	0.755	0.923
2	4.645	.935	.883	.779	.920
3	8.213	.982	.864	.820	.919
4	12.00	.883	.899	.730	.927
Overall	12.00	-----	0.883	-----	0.920

flow rates if required. Most of the remaining characteristics resulted from the objective of designing a multistage compressor with a high-efficiency potential at an elevated loading level.

The initial step in the preliminary design of the four-stage, high-pressure compressor (HPC) was taken by using a meanline program incorporating the loss and peak pressure-rise models previously presented. This program also includes estimates of hub and casing vector diagrams assuming an isentropic simple radial equilibrium. A conceptual design using state-of-the-practice technology and current design practices was executed first. Then, assuming the postulated technology advancements, an assessment of the performance potential of this design was made.

The meanline program provided the average loss, aerodynamic blockage, and peak pressure-rise capability of each stage of the four-stage configuration. A stagewise distribution of effectivity was prescribed based on the philosophy that the operating points of the front and back stages would primarily pivot about the two middle stages as the compressor is throttled along a typical engine operating line. In addition, the averaged effectivity of the compressor was selected to be consistent with a positive stability margin of about 5 percent at the aerodynamic design speed. The required stability margin depends on the intended application and availability of practical stability-management technologies. Stage effectivity distributions are given in table I, which shows the two middle stages to be the set near their peak loading capabilities.

Of the several flow-path shapes (constant casing, constant meanline, and constant hub) investigated, a constant-diameter casing provided the best balance between high pressure ratio and good efficiency. Because of the need to limit the exit rim speed, the casing diameter was reduced at the aft end of the compressor. A discharge Mach number of about 0.35 was assumed based on

considerations of matching with an additional downstream stage. Stage efficiency was refined by balancing stage reaction, inlet swirl, solidity, aspect ratio, and axial velocity diffusion. Orchestrating all these parameters resulted in an overall total-pressure ratio of 12:1 at a rotor 1 (R1) corrected tip speed of 1477 ft/s. The average aspect ratio of the rotors was 0.8 and that of the stators was 1.0. Aspect ratios for the rotors were governed primarily by aeroelastic stability considerations. The rotor and stator average solidities were about 2.0. The predicted stage-by-stage distribution of polytropic efficiency and compressor overall efficiency is given in table I. Reflected in these efficiencies are the following rotor tip clearance levels: 0.020 in. for R1, 0.018 in. for R2, 0.016 in. for R3, and 0.014 in. for R4. An evaluation of current and near-term core compressor clearance trends supported the assumed clearance levels. The first three stators are cantilevered from the casing with an average hub clearance of 0.018 in. These hub clearances and other clearances for anticipated variable stators were factored into the efficiency predictions. The overall performance quoted for the four-stage HPC extends from the guide-vane leading edge to the compressor discharge.

The flow path displayed in figure 8 was biased towards high work and high efficiency. A variable-stagger inlet guide vane (IGV) provides part-speed operability. The guide vane is intended to deliver a nominal swirl distribution of 9° counterswirl at the hub, 2° counterswirl at midheight, and 0° at the casing. This choice was made to control the rotor 1 hub reaction and to reduce the absolute Mach number at the inlet to the stator 1 hub. Note that the stator leading edges are swept forward near the endwalls to tailor the loading in those regions. There are 32 inlet guide vanes, 54 first stators (S1), 74 second stators (S2), 132 third stators (S3), and 104 fourth stators (S4). The rotor blade counts are 26 R1's, 56 R2's, 76 R3's, and 80 R4's. Preliminary estimates of off-design performance, assuming current technology, indicate a potential
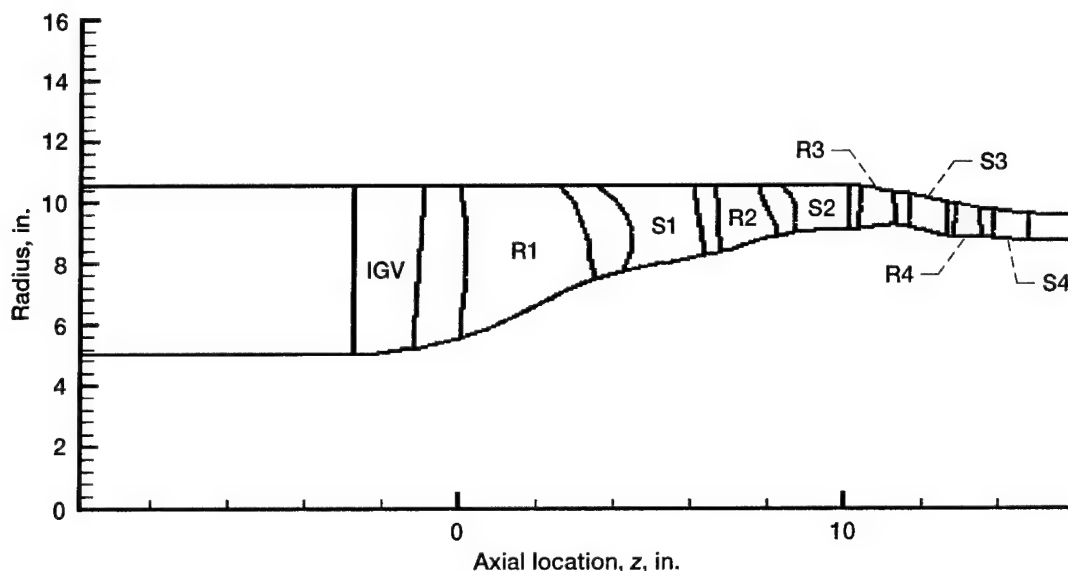
Figure 8.—High-pressure compressor flow path.

need for variable S1, variable S2, and interstage bleed between the second and third stages.

The ultimate performance potential of the previously described state-of-the-practice design was evaluated by incorporating the anticipated advanced aerodynamic technologies in the meanline program. The results shown in table I indicate a significant increase in overall efficiency in addition to a higher stability margin for the same duty. Thus, the advanced technology goal displayed in figure 6 was set.

Throughflow.—After selecting the aerodynamic design point and verifying that the basic geometric parameters derived from the meanline analysis had the potential to be developed into a viable configuration which satisfied the prescribed technical goals, the spanwise tailoring of the vector diagrams was begun by using an adaptation of the inverse throughflow computer program described in reference 16. The tailoring involves an iterative loop between an intrablade mean-stream surface analysis and a blade geometry generator. The computations are based on the streamline curvature method with the inclusion of an axisymmetric body force field assumed to act normal to the surface formed by the stacked camber lines of each blade row. Custom-tailored airfoils were employed for all blade rows. The airfoil customization technique used consists of assuming the meridional distributions of total pressure through the rotors and of angular momentum through the stators. Then, after correcting for departures from the mean camber line, airfoils are fitted to the calculated relative flow angles and a two-part, quarter-sine-wave thickness

distribution. The stream surface sections are stacked along a specified backbone or stacking axis to obtain three-dimensional blade surfaces.

A process of successive refinement guided by CFD results determined the incidence and deviation angles used to generate the airfoil sections. Initial values were estimated using the quasi-three-dimensional, viscous code RVCQ3D (ref. 17). RVCQ3D was also used to direct the initial selection (meridional distributions of angular momentum or total pressure within blades) of airfoil contours. These contours were updated by conducting isolated blade-row viscous analysis using ADPAC (ref. 18) with inflow and outflow boundary conditions extracted from the throughflow analysis. The results from the ADPAC analysis were also used to tailor the stacking axis and to modify vector diagrams to control spanwise static-pressure gradients. Spanwise distributions of blade-row losses were also revised using the CFD results as a guide. Aerodynamic blockages were initially taken from the meanline program and were successively adjusted based on CFD results.

Setting the compressor discharge Mach number and total-pressure ratio fixes the overall static-pressure rise. With the flow path fixed, the meridional static-pressure gradient is primarily determined by the stage effectivity distributions derived from the meanline analysis. The wall static-pressure distributions established with the throughflow analysis at the aerodynamic design point are displayed in figure 9. To achieve low loss and to ensure aerodynamic stability, it is generally desirable to minimize static-pressure gradients along the endwalls.
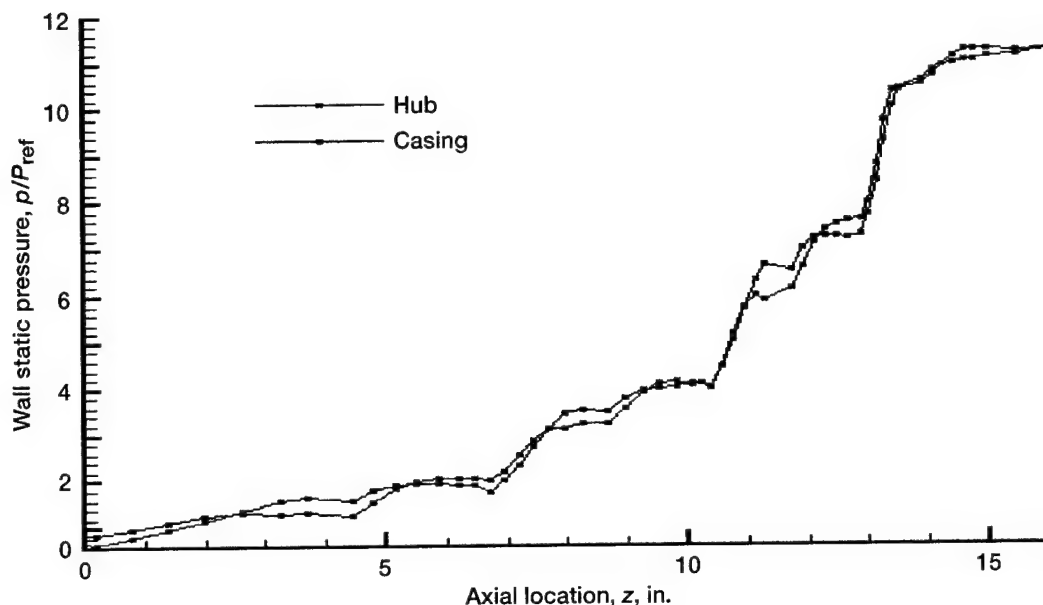
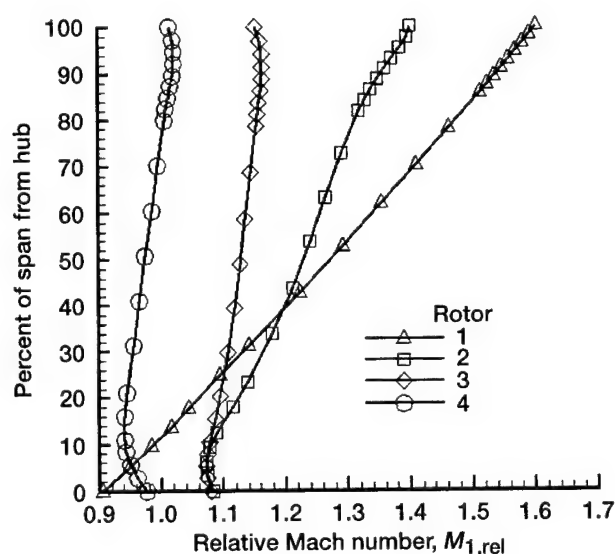Figure 9.—Wall static-pressure distribution at aerodynamic design point.

Figure 10.—Rotor inlet relative Mach number.

Figure 11.—Stator inlet absolute Mach number.

Figure 9 shows that the meridional gradients of static pressure are approximately constant through most of the rotor blade rows (see fig. 8 for blade locations) and then taper off toward the trailing edge. The static-pressure rise is more rapid in the front half of the stator blade rows and quickly tapers off in the remaining half of the blade. For all blade rows, preferential radial forces were introduced through the tangential leaning of the mean camber surface to control spanwise gradients of static pressure.

Spanwise variations of the rotor inlet relative Mach number are shown in figure 10 for all four rotors at the aerodynamic design point. For rotor 1, the relative Mach numbers vary from high subsonic near the hub to 1.6 near the casing. The two middle rotors (R2 and R3) have supersonic inlet Mach numbers across the span, which makes stage matching exceptionally difficult. The rotor 4 inlet Mach numbers are approximately sonic across the span. The inlet absolute Mach number distributions for the stators are displayed in figure 11. The stator 1 hub Mach number is slightly above sonic with all remaining stators having subsonic inlet Mach numbers.
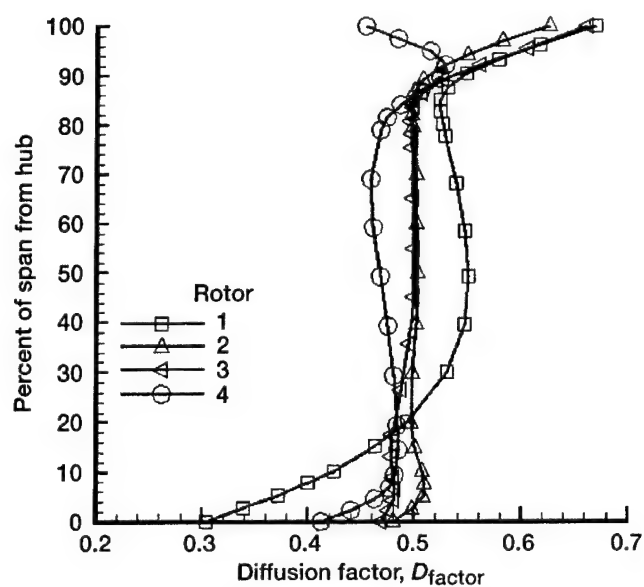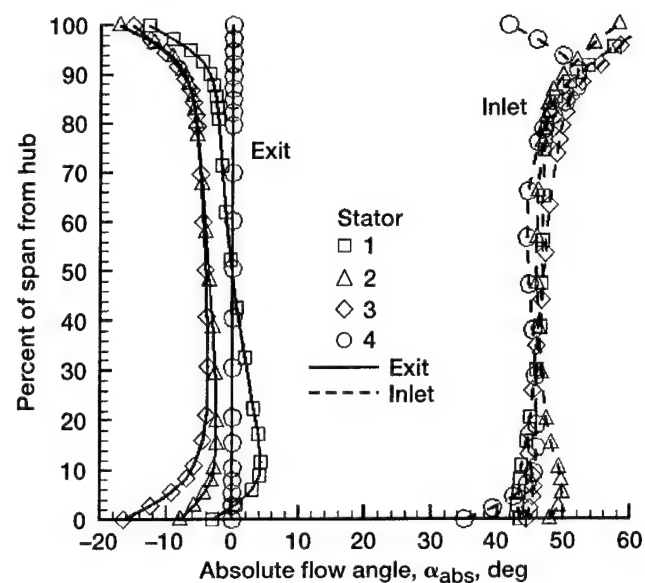
Figure 12.—Rotor diffusion factors.

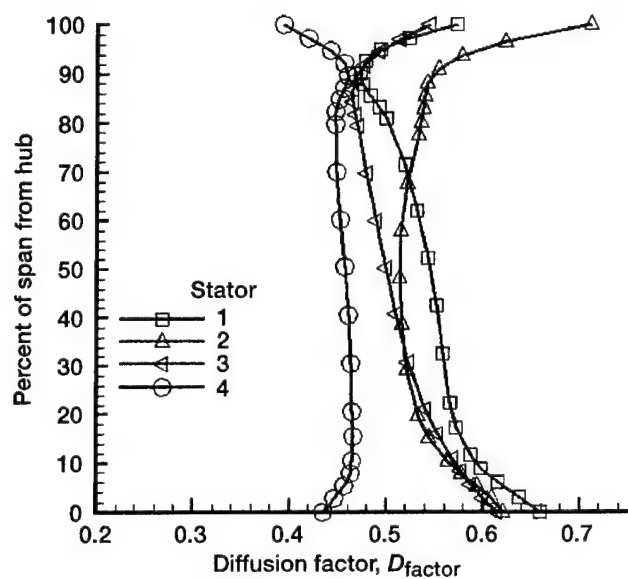Figure 14.—Stator inlet and exit absolute flow angles.
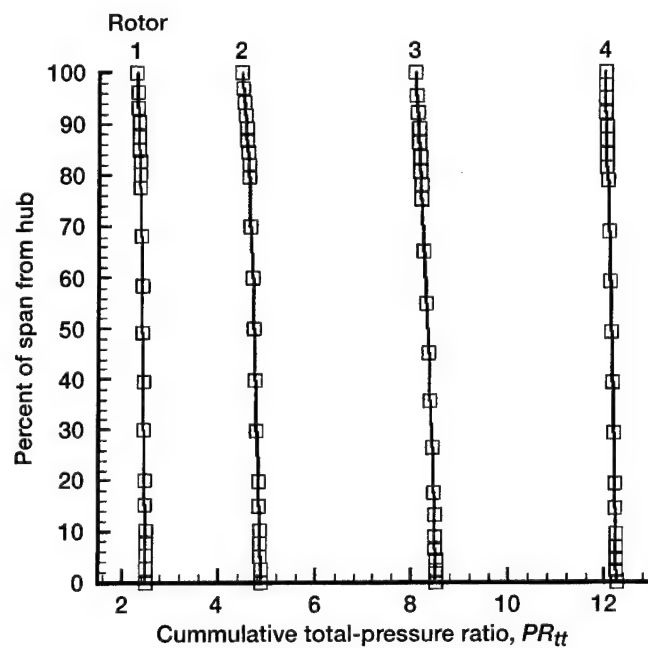

Figure 13.—Stator diffusion factors.

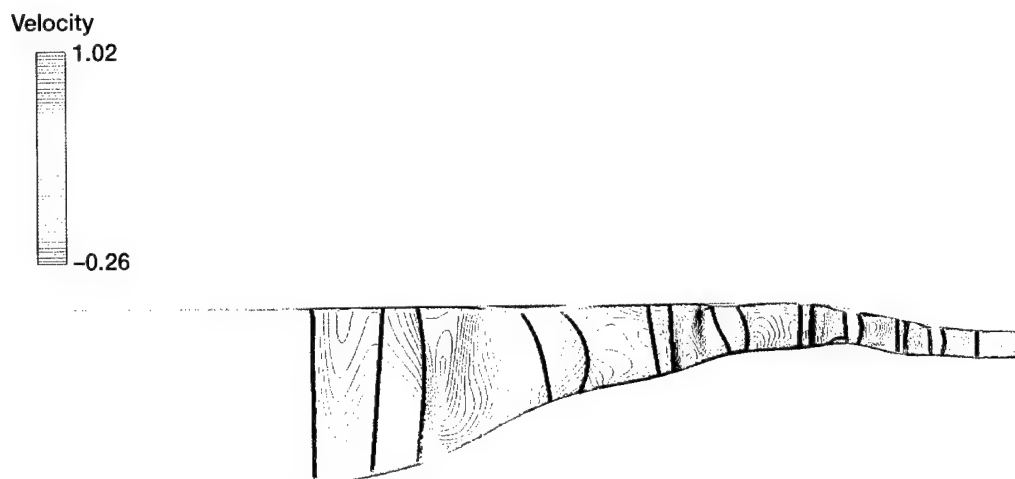Figure 15.—Rotor exit cumulative total-pressure ratio.

Figure 16.—Axisymmetric averaged throughflow velocity distribution at aerodynamic design point.

The spanwise distributions of the diffusion factor D_{factor} for rotors and stators at the aerodynamic design point are shown in figures 12 and 13, respectively. These diffusion factors are locally high, reflecting the increased stage aerodynamic loadings. The maximum diffusion factors are in excess of 0.65 and occur near the endwalls. However, the average values are not far from levels for which acceptable performance has been demonstrated. The stator inlet and exit absolute flow angles are plotted in figure 14. On the average, approximately 50° of turning was achieved in the stators. The intent was to overturn near the endwalls to accommodate secondary flows.

Counterswirl (swirl opposite the direction of rotor rotation) was prescribed for S2 and S3 to control the spanwise distributions of rotor (R3 and R4) aerodynamic loading, as defined by the diffusion factor. This counterswirl also increases the stage reaction, which may have a favorable impact on stage performance. Spanwise distributions of cumulative rotor exit total-pressure ratios are displayed in figure 15. These distributions are compatible with the prescribed stator exit swirl profiles. The intent was to propagate a hub-strong, total-pressure profile within the multistage. Such a profile was thought to be favorable with respect to aerodynamic stability as the machine is throttled. Overall, the vector diagrams were tailored under the guidance of CFD results to provide a beneficial relief to the high-loss and high-loading endwall regions.

The initial blading was generated and refined using isolated blade-row CFD analysis. The axisymmetric averaged throughflow velocity distribution at the aerodynamic design point is presented in figure 16. This was processed from the results of a three-dimensional multistage simulation employing a mixing plane approach within the ADPAC code. The results serve to identify in the design potential weak points that are in need of further refinements. Evident from the figure is that in the hub region of R3, there is weak flow caused by the high aerodynamic loading being requested and by aerodynamic mismatching between blade rows. In addition, the rotor tips show flow weaknesses associated with leakage flow development in a high-loading region with shocks. Based on the results from the multistage ADPAC simulation, the overall performance potential of this preliminary design configuration was predicted to be a pressure ratio of 12:1 at a polytropic efficiency of 89 percent. To further appreciate the level of technical advancement being sought, figure 17 shows the fully developed compressor goal relative to established performance trends. This design sits at an average work factor of 0.44. It can be observed that the preliminary design results are in line with current trends and that achievement of the goal would indicate a substantial advancement over the state of the practice if not over the state of the art. What is not explicitly stated is the suitability of such a design for a practical engine product. Further research and development are required to ascertain the postulated aerodynamic technology advancements.
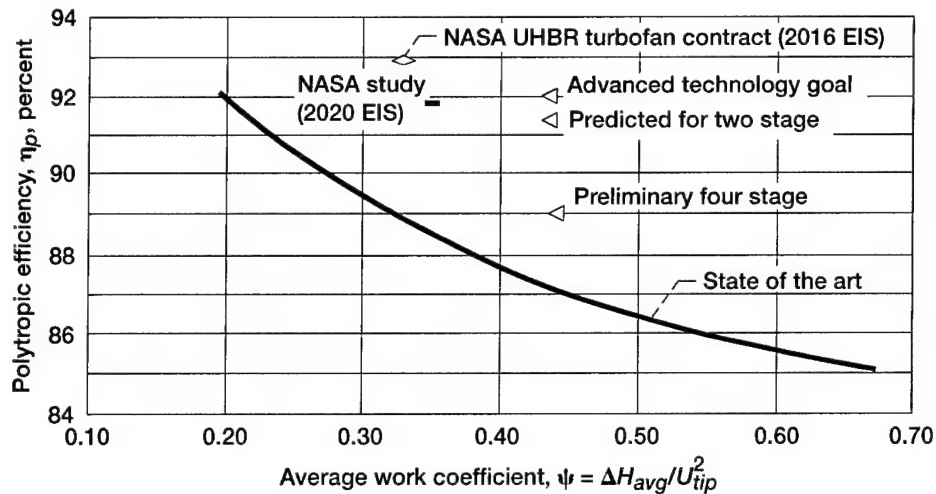
Figure 17.—Core compressor technology assessment in terms of work factor and polytropic efficiency. UHBR, ultra-high bypass ratio; EIS, entry into service.

Part II: Three-Dimensional Blading Development

Three-Dimensional Inverse Method

The primary prescribed quantities in the three-dimensional inverse method are the blade stacking line $f_{stack} = f_{stack}(r)$, the blade thickness distribution $T = T(r,z)$, and the blade pressure-loading distribution $\Delta p = \Delta p(r,z)$. Herein, blade pressure loading is defined as the pressure difference between the blade upper and lower surfaces at fixed axial positions. For a given set of inputs, the three-dimensional inverse method computes the corresponding blade mean camber surface $f = f(r,z)$. Clearly, the blade geometry corresponding to prescribed values for $[f_{stack}, T, \Delta p]$ is not guaranteed to have the optimum performance or to be aeromechanically acceptable. The challenge is to pick these quantities to arrive at a satisfactory blade.

The three-dimensional inverse method is based on the solution of the Navier-Stokes equations using the robust, finite-volume, time-marching scheme of Jameson, Schmidt, and Turkel (ref. 19). Viscous effects are modeled using the method proposed by Denton (ref. 20) for turbulent flows as adapted by Damle (ref. 21). During the time-marching process, fluid is allowed to cross the blade surfaces, and a pressure-jump condition (blade pressure loading) is imposed across the blade surfaces. The "flow-tangency" condition along the blade surfaces is then used to update the blade geometry. Endwall clearances are modeled by assuming periodicity within the clearance

gap. The INV3D computer code employed in this study can run in either the standard analysis mode or the inverse mode.

The successful strategy employed in the previously published work on this three-dimensional inverse method (ref. 22) was used to pick the prescribed quantities $[f_{stack}, T, \Delta p]$ that would improve the present transonic rotor blade designs. The strategy is as follows:

1. Start with blade geometry obtained with the traditional design tools (e.g., meanline and/or throughflow method). This geometry is termed the "original design." Then switch to the three-dimensional inverse method to improve the geometry, using the original design as the initial guess.

2. Input to the three-dimensional inverse method the blade tangential thickness distribution, which has been kept the same as the original design to satisfy some structural constraints and to reduce the number of degrees of freedom.

3. Adjust the blade pressure loading $\Delta p(r,z)$ to introduce geometric features that enable the control of local flow structures (shock, secondary flows, boundary layers, etc.) linked to a performance index. The choice of the blade pressure loading is a three-dimensional approach. At a given spanwise station, the blade pressure-loading distribution is used to manage the local aerodynamics and to tailor the spanwise vector diagrams:

$$\int_{le}^{te} r\Delta p \, dA_\theta \approx \dot{m}\left[\left(r\overline{V}_\theta\right)_{te} - \left(r\overline{V}_\theta\right)_{le}\right] \quad (1)$$

14   NASA/TP—2002-211568

where the subscripts *te* and *le* are trailing edge and leading edge; A_θ is the tangential projection of the blade surface area; $\dot{m}$ is the mass flow rate; and $\overline{V}_\theta$ is the mass-averaged tangential velocity. For a rotor, specifying the blade pressure loading at every spanwise station is the same as prescribing the spanwise distribution of total temperature rise across the rotor. This is the usual two-dimensional thinking when a two-dimensional inverse method is used. With a three-dimensional method, an additional control is the spanwise variation of the blade pressure loading. As will be described shortly, this is used to adjust the orientation of the passage shock as seen in a meridional plane.

4. Modify as needed the prescribed blade stacking line so as to restrain potential endwall corner separations and to limit excessive blade twisting.

The blade design procedure proposed herein is very compatible with the inverse throughflow method used in part I to generate the original blades. In particular, the design intents, as described by the spanwise profiles of axisymmetric averaged pressure, temperature, and angles, are fed into the inverse method as inflow and outflow boundary conditions. One of the main advantages of using a three-dimensional inverse method is that the critical physics of the complex aerodynamic interactions are directly accounted for rather than being patched in a somewhat convoluted fashion.

Reblading Using INV3D

The front two stages, including the inlet guide vane, of the four-stage configuration were extracted for a more refined aerodynamic design. A meridional cross section of the flow path is shown in figure 18. The following are the aerodynamic design requirements for the two stage: a corrected flow of 70 lbm/s, an overall total-pressure ratio of 4.645:1, and a rotor 1 corrected tip speed of 1477 ft/sec. From part I, the state-of-the-practice efficiency potential of this configuration was estimated to be 89 percent polytropic. The intended axisymmetric profiles and design considerations for the original blades are found in part I.

In this section, the redesign of the second rotor (R2) is discussed in detail for three important reasons. First, the second rotor is the most challenging because the incoming relative Mach number is supersonic from hub to tip. Second, the relative aerodynamic loading based on the effectivity parameter E is the highest. Third, this rotor is
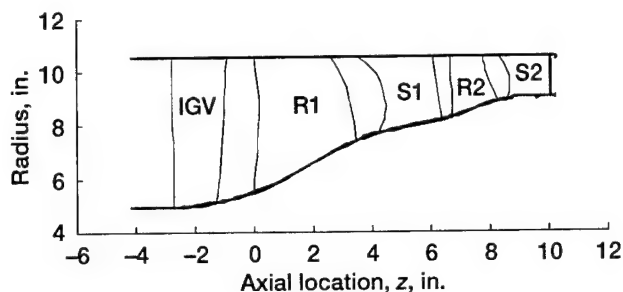

Figure 18.—Flow path for two-stage high-pressure compressor.

also critical in terms of proper stage matching because of possible strong interactions with the upstream stator.

The design intents are obtained from the throughflow model, which is updated based on information supplied by the multistage CFD simulations to be described in the section Multistage Performance Evaluation. It is not possible to get an exact match between the present throughflow and the axisymmetric average of the CFD solution because of inconsistencies in formulation. Nevertheless, an acceptable match was achieved. At the inlet, the spanwise distributions of total pressure, total temperature, and flow angles are specified. The design intent spanwise distribution of static pressure is prescribed downstream. Since the present formulation of the inverse problem called for the specification of the blade pressure loading, which is directly related to the spanwise distribution of total temperature rather than to the total pressure, adjustments to the magnitude of the blade pressure loading were sometimes required to match the design intent exit total-pressure distribution and the mass flow rate.

For this reblading exercise, the meridional envelopes of the blade were fixed. The blade pressure loading was carefully constructed with the following scheme. Figure 19 shows the contour of the pressure loading of the
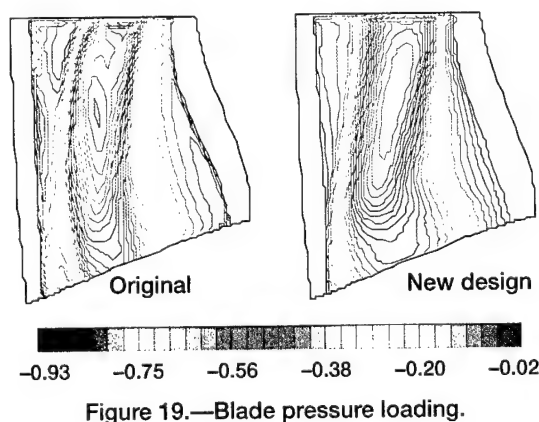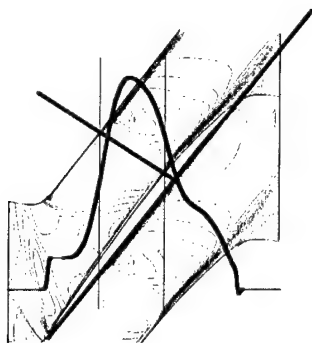

Figure 19.—Blade pressure loading.

Figure 20.—Axial loading
distribution.

Figure 21.—Passage shock positioning in meridional plane.

original blade at the design intent backpressure (left contour plot). Two distinct discontinuities spanning from hub to tip are clearly indicated. The axial distribution of the blade pressure loading superimposed on the Mach number contours in the blade-to-blade plane at the same span location (near tip region) is shown in figure 20. Note that the two near discontinuities in the blade loading distribution conform to the location of the passage shock. The front discontinuity corresponds to the passage shock impinging on the pressure surface of the blade above it, whereas the back discontinuity corresponds to the passage shock impinging on the suction surface of the blade below it. Looking back to figure 19, note that the passage shock is rather strong at the upper half of the blade and hence there exists a potential for tailoring the pressure-loading distribution to weaken it, as has been demonstrated in previous work (ref. 23).

Another important consideration is the placement and orientation of the passage shock as seen in the meridional plane. At the design point, the passage shock should reside inside the blade passage, and its orientation should be such that it has maximum obliquity relative to the incoming flow to minimize shock loss (shock sweep). This suggests that the passage shock near the tip region should be placed as far back as possible (i.e., the passage shock impinging on the suction surface near the trailing edge), whereas it should be as far forward as possible at the other end (the passage shock impinging on the pressure surface near the leading edge). After the desired shock position in the blade passage is selected, it is possible to estimate where the passage shock intersects the blade surfaces based on the geometry of the blade passage (the blade stagger angle and the blade spacing).

There are a number of different aspects to the selection of pressure loading for transonic blades. First, the selection of loading shape and magnitude in the entrance region of the blade translates into tailoring the aerody-
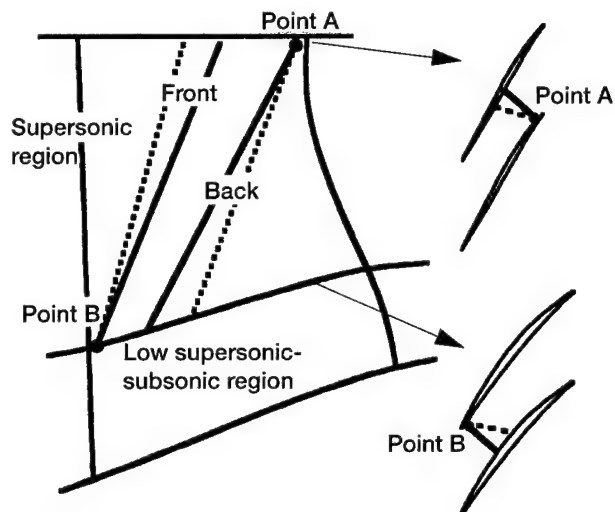
namic surfaces for the proper supersonic wave pattern and throat area. This tailoring is a means for achieving the required mass flow rate with a started shock configuration. Additionally, the selection of shock position on suction and pressure surfaces as well as its strength must be carefully crafted to obtain low losses. After the shock position in the meridional plane has been selected, one of the loading discontinuities is fixed at that span position (points A and B in fig. 21). The other discontinuity can be placed to introduce some obliquity of the shock in the blade-to-blade plane. As part of the selection of the meridional shock position, the region encompassing the passage shock must also be determined. The tip of the blade sets the first spanwise location and the second is chosen to be where the inlet relative Mach number is slightly above unity. This positioning divides the blade into the low supersonic-subsonic region where smooth loading shapes can be used without producing discontinuities in the blade and the supersonic flow portion where the discontinuities in loading must be prescribed to obtain "smooth" blade shapes (fig. 21).

The strength of the shock can be controlled somewhat through the specification of the severity of the pressure-loading gradient. A steep gradient will produce a strong shock with a greater shock loss and a potentially greater risk of shock-induced, boundary-layer separation. However, there are limits as to how much the shock can be weakened and how much obliquity can be introduced in the blade-to-blade plane. If the shock is weakened past a certain point, the resulting blade will have a "kink" that may lead to poor performance at off-design conditions. The second limit, blade-to-blade shock obliquity, is
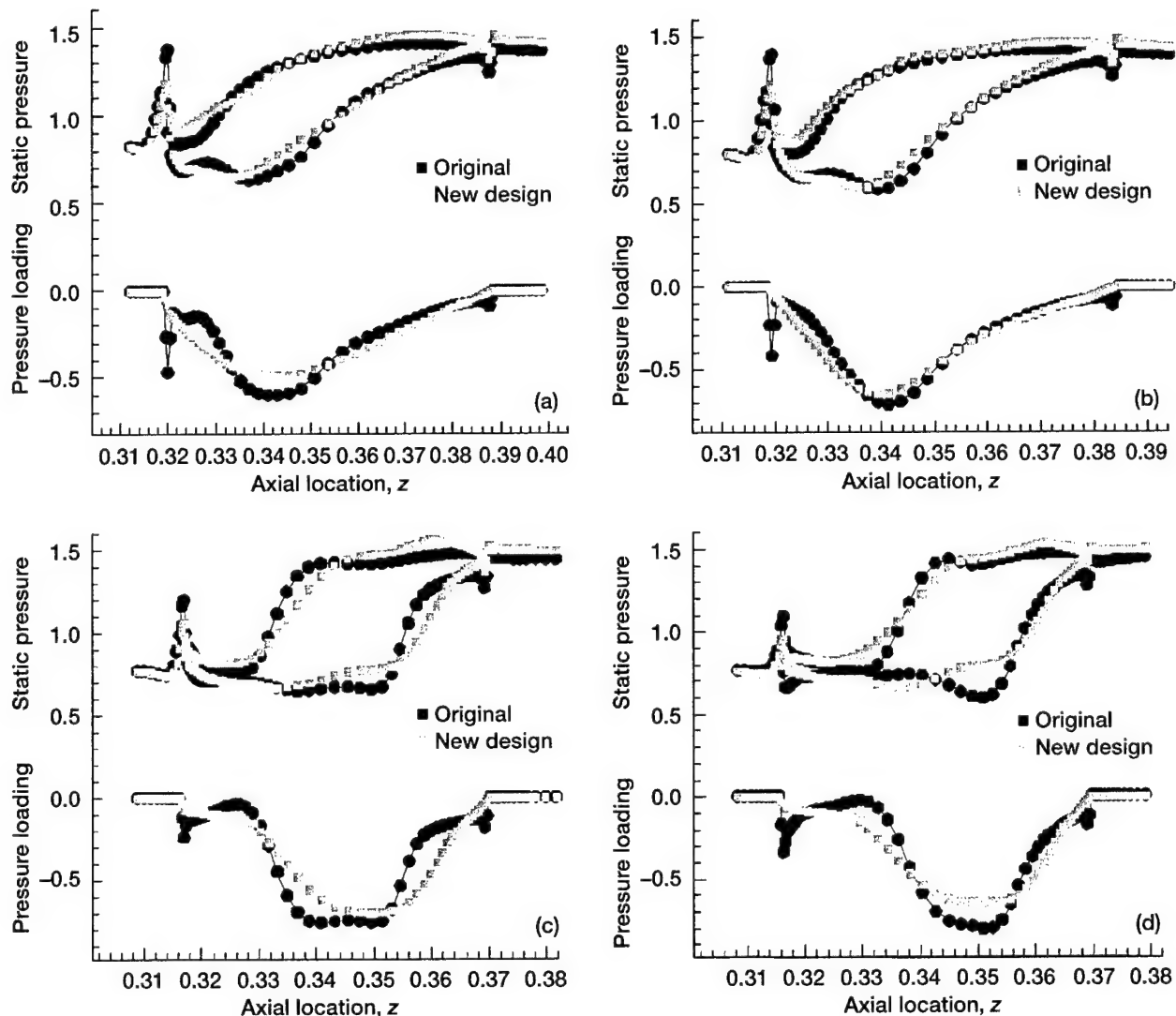
Figure 22.—Blade-surface pressure and loading distributions for several span sections. (a) Near the hub. (b) Below 50-percent span. (c) Above 50-percent span. (d) Near the tip.

observed when the two discontinuities have been placed too far from one another (dashed line in fig. 21). In such a case, the shock will occur at the specified location on the pressure surface (front discontinuity, see fig. 21) but will impinge on the suction surface at a location upstream of the "specified" back discontinuity, resulting in too much loading in the subsonic diffusion portion of the blade and therefore overcambering the blade in that region. This "manual" adjustment of the blade pressure loading is a delicate process and does require some experience to achieve success.

Figure 19 (right contour plot) shows the blade pressure loading of the redesigned rotor 2. Compared with the original design (left contour plot), the figure clearly

illustrates the weakening of the passage shock and an increase in its obliquity. Figure 22 compares the detailed blade pressure loading (bottom) and pressure distributions on the blade surfaces (top) of the original design and the new design at several spanwise stations. Two important differences between the two designs are worth pointing out. First, the passage shock is weakened at all spanwise stations. Second, the passage shock moves a little forward below the 50-percent-span location while being displaced farther aft above the 50-percent-span location. Recall that the reorientation of the passage shock was purposely created in the specification of the blade pressure loading to increase its obliquity relative to the meridional flow.
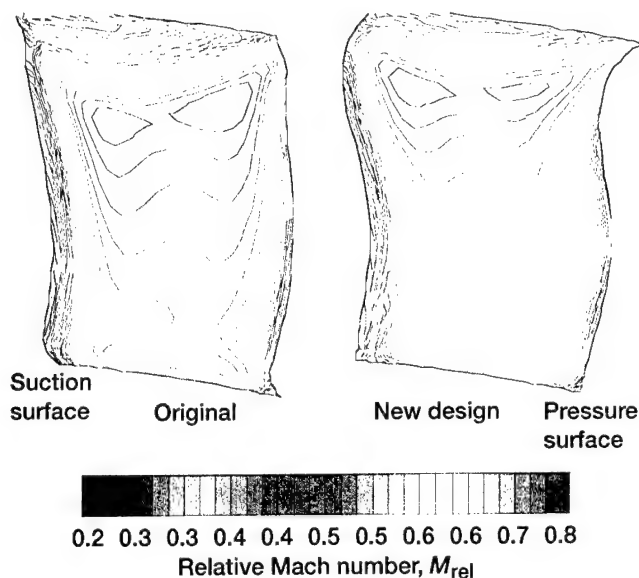
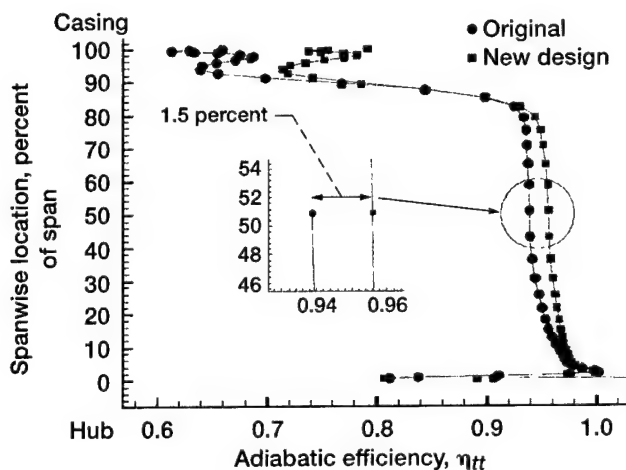Figure 23.—Relative Mach number contours at blade trailing-edge plane.

0.2 0.3 0.3 0.4 0.4 0.5 0.5 0.6 0.6 0.7 0.8
Relative Mach number, M_{rel}

Figure 24.—Comparison of spanwise distribution of adiabatic efficiency at design point.

-1.0 -0.9 -0.8 -0.7 -0.6 -0.5 -0.4 -0.3 -0.2 -0.1 -0.0

Figure 25.—Comparison of pressure loading.

0.2 0.3 0.5 0.6 0.8 0.9 1.0 1.2 1.3 1.5 1.6
Mach number

Figure 26.—Cascade flow near casing.

Figure 23 shows the flow field in a crossflow (r,θ) plane behind the blade trailing edge. The tip clearance-to-chord ratio is approximately 1 percent. For the new design, there is a clear indication of a cleaner endwall flow that is attributed to the weakened passage shock and possibly a modulation of secondary and leakage flows. Note that the new blade geometry is twisted differently near the casing endwall, whereas the original blade was stacked so that its leading edge is swept forward relative to the flow. This new twist introduces a component of blade force that restricts unfavorable spanwise flow migrations. The figure also shows that the blade wake for the new design is
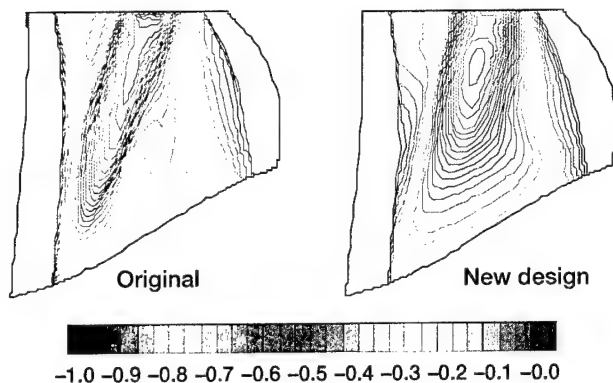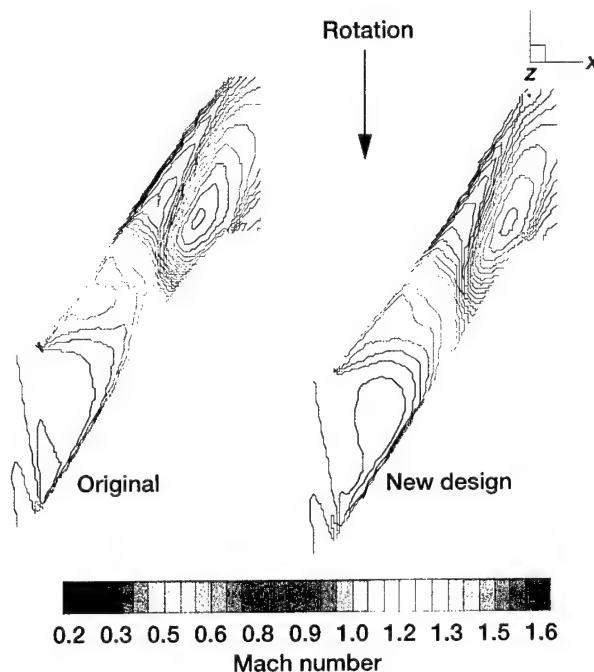
slightly thinner over the entire span. The Navier-Stokes solver ADPAC (ref. 18) was used to independently confirm the improved flow field and performance of the new design. The calculation used a mesh size of 90×48×40 (a total of 172 800 cells) that included 4 cells in the tip clearance region. At the design intent backpressure, the ADPAC solution predicted an overall adiabatic efficiency improvement of 2 percent over the original design running at the same backpressure with approximately the same flow rate. Figure 24 shows the spanwise distribution of adiabatic efficiency as predicted by ADPAC. It can be observed that efficiency improvements are found over the

Figure 27.—Visualization of rotor blades generated with INV3D.

entire span, with about 1.5 percent over the core flow and over 10 percent in the casing endwall.

The first rotor (R1) was also revised using the same pressure-loading scheme. Figure 25 compares the blade pressure loading of the original design (left contour plot) with that of the new design (right contour plot), and figure 26 presents the blade-to-blade flow field near the tip. As in the second rotor (R2), the passage shock was weakened and slightly reoriented to increase shock obliquity. The performance of R1 (as predicted by ADPAC) showed an improvement of 1.5 percent in adiabatic efficiency over the original design.

In summary, the transonic rotor blades generated by INV3D using the present pressure-loading strategy indicated a relatively higher efficiency potential than the original blades. Stacking and thickness distributions were fixed according to the original blades. Perhaps a combination inverse direct method can be used to explore other degrees of freedom. Preliminary mechanical and structural assessments of the inverse-designed blades thus far appear promising. The blades are curvier than usual, having forward-swept leading edges (fig. 27). Implications for this design freedom, from the perspective of product development and total cost, are beyond our scope. Similar to the rotors, a pressure-loading strategy can be developed for subsonic stators, but this is reserved for future work. The stators were designed as described in part I and were matched to the rotors solely based on CFD simulations. Additional geometric information for all blade rows is given in appendix A.

Multistage Performance Evaluation

Procedure.—To verify the improved performance potential of the rebladed two stage and to facilitate stage matching, the multistage CFD code APNASA, based on the formulation of Adamczyk (ref. 5), was employed. The APNASA code computes the time-mean flow as seen by an average passage of a blade row imbedded in a multistage environment. Details of the numerics, turbulence model, and deterministic stress closure are given by Adamczyk et al. (ref. 24). This code has undergone extensive validation and/or calibration (refs. 25 and 26) and has been found to be a reliable predictive tool for multistage aerodynamics. In executing the design, APNASA, ADPAC, and INV3D were integrated in the iterative design loop. The procedure is as follows:

1. From the throughflow model, extract the inflow and outflow boundary conditions for INV3D. Rotor blades are designed using INV3D with the pressure-loading strategy previously described; the stators are designed according to the inverse throughflow method outlined in part I.

2. ADPAC is used to fine-tune the individual blade-row designs while holding the inflow conditions extracted from the throughflow model. The exit profiles from the individual blades are checked against the design intent and the blades are redesigned as in step 1 should the exit profiles or losses be far too different from those of the throughflow.

TABLE II.—PREDICTED PERFORMANCE POTENTIAL
AT AERODYNAMIC DESIGN POINT

Inlet correct flow, Wc, lbm/s 71.2
Overall total-pressure ratio, PR_{tt} 4.65:1
Corrected mechanical speed, Ω, rpm 16 060
Overall efficiency, percent
Adiabatic, η_{tt}..90.36
Polytropic, η_p...92.19

3. The multistage aerodynamics of all the blade rows
are predicted with APNASA. An interrogation of the
APNASA solution is made to arrive at appropriate revi-
sions for the throughflow (i.e., aerodynamic blockage,
loss and turning distributions) model and the blade design
strategies (incidence, trailing-edge loading distribution,
and stacking).

The above steps usually converge after two to three
design iterations. Note that step 3, involving mainly
APNASA, is more like a development stage rather than a
design stage. The throughflow model is still at the center
of the overall process and allows all the blade rows to be
designed simultaneously. Additional work is needed to
streamline this procedure and make it more direct.
Perhaps a totally different process with a well-founded
formalism is warranted. In addition, the entire process or
parts of it may be very amenable to various optimization
schemes that can directly accommodate aeromechanical
and manufacturing constraints.

APNASA results.—A sheared H-mesh was constructed
for the two-stage configuration that included the inlet
guide vane. The mesh consisted of 61 streamwise points
on each of the 5 blade rows, 61 spanwise points, and 51
blade-to-blade points for a total dimension of $626 \times 61 \times 51$.
There are four cells in the rotor tip clearances and stator
hub clearances. The clearance gaps were modeled with a
periodic boundary condition rather than with direct
discretization. Different mesh sizes were investigated to
ascertain the sensitivity of the results and to determine the
adequacy of the selected mesh size. Simulations were
conducted at several operating speeds and backpressures.
The results for the simulation closest to the aerodynamic
design point will be presented followed by the overall
characteristics at other operating conditions.

The predicted performance potential at the aerody-
namic design point is presented in table II. The perfor-
mance is determined from computed circumferentially
mass-averaged total pressures and temperatures at recti-
fying planes situated midway between the individual
blade rows. The overall performance quoted in the table

TABLE III.—DESIGN POINT STAGE
PERFORMANCE POTENTIAL
PREDICTED BY APNASA

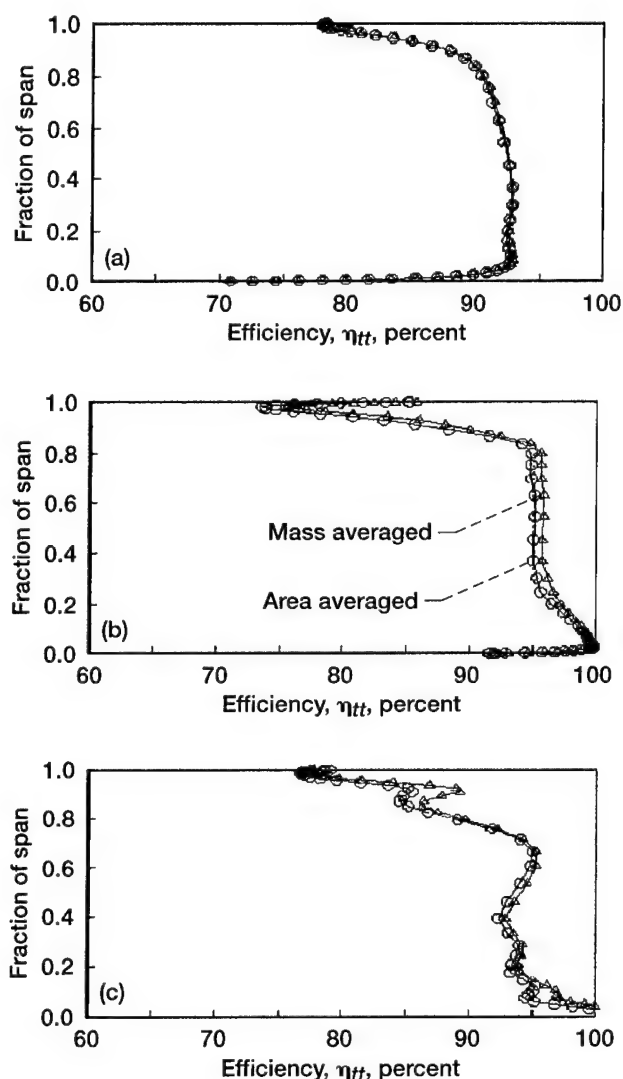| Stage	Rotor		Stator
	Total-pressure ratio, PR_{tt}	Polytropic efficiency, η_p, percent	Total pressure loss, $\Delta P_t/P_t$, percent
1	2.423	95.100	1.636
2	1.995	94.420	1.725

Figure 28.—Predicted spanwise variations in adiabatic
efficiency at aerodynamic design point. (a) Overall.
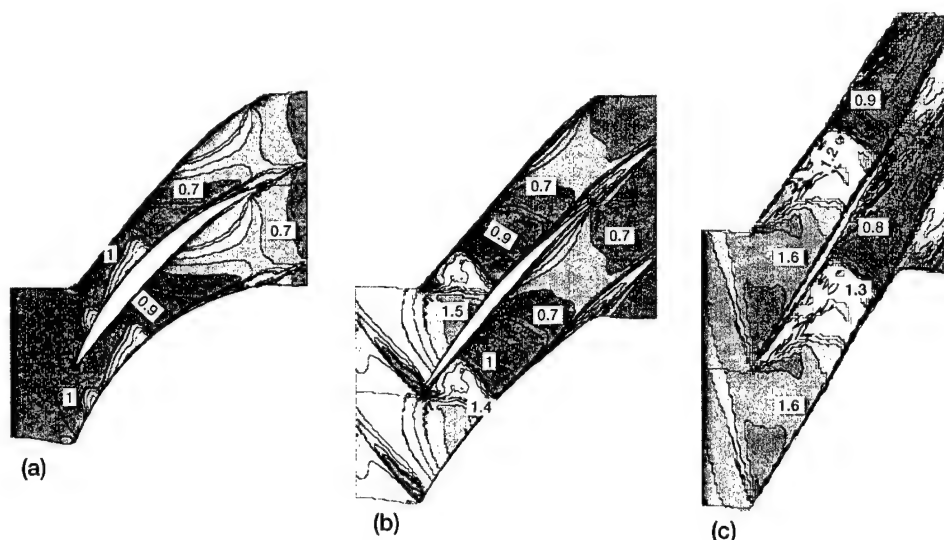(b) Rotor 1. (c) Rotor 2.

Figure 29.—Relative Mach number distributions at design point for rotor 1. (a) 9-percent span. (b) 50-percent span. (c) 95-percent span.

extends from the IGV inlet to one meridional chord downstream of S2. The total pressure loss across the IGV is $\Delta P_t/P_t = 0.476$ percent. A summary of the stage-by-stage performance potential is given in table III.

At the design corrected speed and pressure ratio, the predicted mass flow rate is approximately 1.7 percent higher than the design intent. The polytropic efficiency significantly exceeds the state-of-the-practice value indicated in part I and is, in fact, at a level consistent with the four-stage advanced technology goal. The design-point overall performance potential for the rotors is exceptionally good in terms of efficiency. The spanwise variations of adiabatic efficiency for R1, R2, and the overall two stages are plotted in figure 28. It is evident that the efficiency of R1 is relatively high over the lower 80-percent span and rapidly drops off in the remaining 10-percent span near the casing. A similar trend is observed for R2, except that the efficiency levels are somewhat lower between 20- to 50-percent span. The distribution of efficiency for the overall two stages, extracted one meridional chord aft of S2, indicates a good distribution across most of the span with a gradual dropoff near the casing. Additional spanwise profiles of axisymmetric averaged flow properties are given in appendix B.

The APNASA results at the aerodynamic design point were interrogated to identify the major flow features responsible for the aerodynamic character of the blading and to synthesize their relative impact on performance. The cascade plane relative Mach number distributions for R1 at near hub (9-percent span), midspan, and near tip (95-percent span) are shown in figure 29. Near the hub,
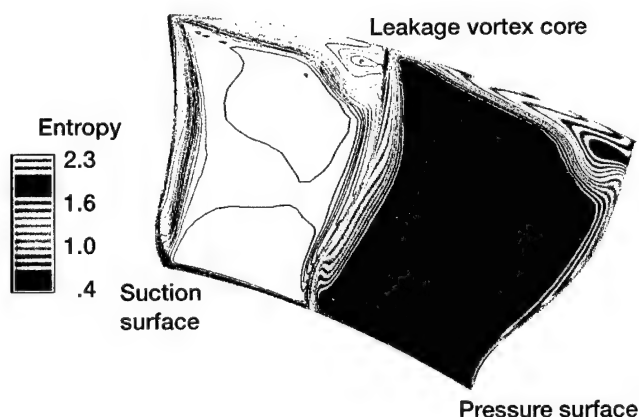

Figure 30.—Entropy distribution at trailing-edge plane of rotor 1.

a rapid diffusion from about 40-percent chord without any shock is observed within the passage, which is consistent with the intended pressure loading shown in figure 25 and does not appear to adversely impact the viscous layers because of the favorable spanwise sweeping of low-momentum fluid near the hub. At midspan, an oblique shock exists in the passage at about 40-percent chord, and the subsonic diffusion in the aft section thickens the suction-surface boundary layer near the trailing edge. The low-momentum fluid in this region centrifuges outward and accumulates near the tip. A cesspool, fed by this process and augmented by the leakage flow, is observed at the blade tip near the pressure side corner. Further evidence of this cesspool is shown in figure 30, which corresponds to the entropy distribution at the
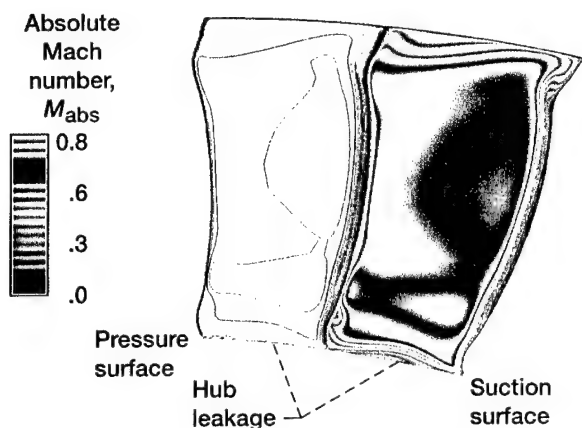
Figure 31.—Absolute Mach number distribution at trailing-edge plane of stator 1.

trailing-edge plane of R1. Near the tip, note the existence of a double shock (evident in fig. 29) that is inconsistent with the intent shown in figure 25. This double shock is perhaps an indication of a deficiency in the viscous treatment of the inverse method and is under investigation. Nevertheless, the flow structure indicates a relatively clean flow conducive to a high-efficiency potential.

The absolute Mach number distribution at the trailing edge of S1 is shown in figure 31. Note the low-momentum region at the hub resulting from the interaction of the hub leakage with the endwall flow. There is indication of a thin wake in the core region. Because of the hub clearance and the local orientation (e.g., sweep and dihedral) of the blading near the endwalls, there is a tendency for low-momentum fluid on the blade surfaces to migrate into the core region, hence the appearance of a relatively thinner wake near the endwalls.

Figure 32 shows the distribution of the relative total pressure at several cross-passage planes from the leading edge to the trailing edge of R2. Evident is the development of the boundary layer on the suction surface along with the evolution of a low-energy cesspool associated with shock-endwall viscous interaction and tip clearance leakage in the casing endwall region. A band of low relative total pressure can be observed at the hub, indicating a weak flow due to excessive diffusion imposed by the blading. Although not explicitly shown here, a strong interaction exists between the bow shock emanating at the leading edge of R2 and the suction-surface boundary layer at the trailing edge of S1. This interaction leads to a local underturning of the stator core flow. However, there does not seem to be any adverse effect on the swallowing capacity of R2 or on the overall matching of the two stages.
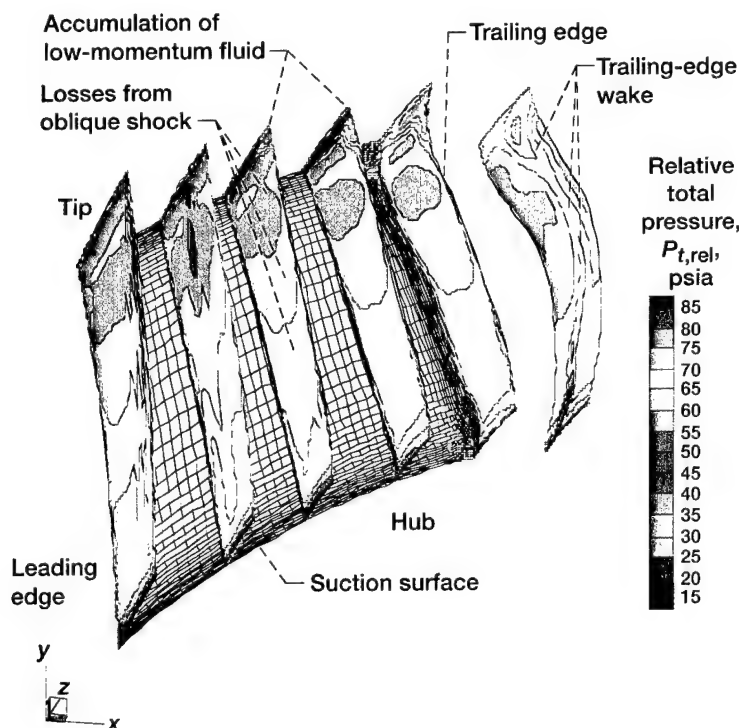

Figure 32.—Relative total-pressure distribution on several cross-passage planes for rotor 2 (courtesy of ASE Technologies, ref. 27).
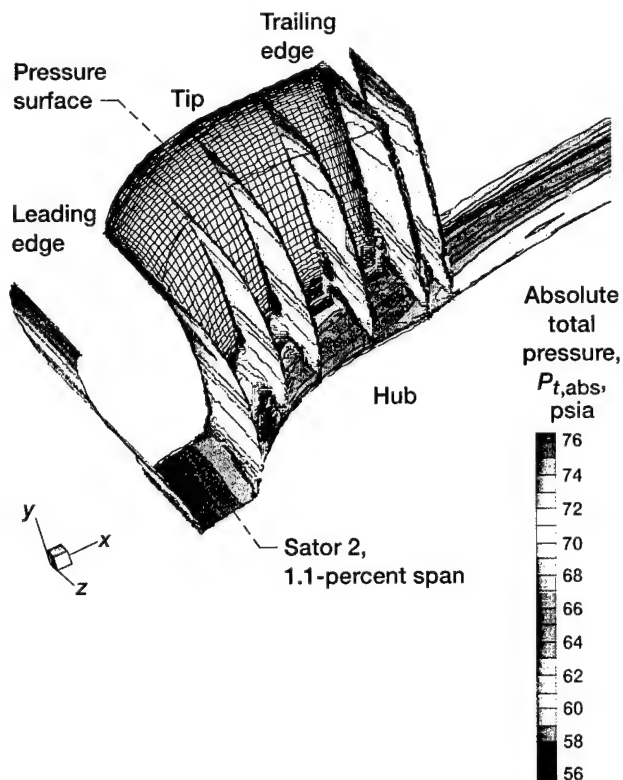
Figure 33.—Absolute total-pressure distribution on cross-passage planes through stator 2 (courtesy of ASE Technologies, ref. 27).

Zone
01 Purple
02 Red
03 Green
04 Blue
05 Teal
06 Orange

Figure 34.—Zonal decomposition of rotor 1 flow domain for assessment of entropy production.

Zone
07 Red
08 Green
09 Blue
11 Orange
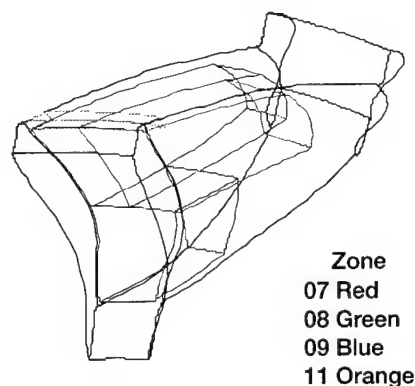
Figure 35.—Additional zones for assessment of rotor 1 entropy production.

The distribution of absolute total pressure at several cross-passage planes from the leading edge to the trailing edge of S2 is presented in figure 33. Clearly evident is the development of the hub leakage flow and its interaction with the endwall blading. A hub-strong, total-pressure profile exists at the inlet to S2 and is rapidly degraded by this process.

A loss audit was performed on R1 to identify sources of entropy generation and their relative contribution to the rotor overall inefficiency. The approach selected for the loss audit was to create the postprocessing tool DISECT-N (ref. 27) that can decompose the spatial domain of a blade passage into zones encompassing selected flow features and entropy generation mechanisms. Entropy fluxes are summed over the boundaries of each zone and the results used as a direct measure of the entropy production within that zone. Note that this tacitly assumes a negligible thermal entropy production. Nine zones (figs. 34 and 35) were selected based on interrogations of the APNASA results; the targeted entropy generation mechanisms are cursorily described as
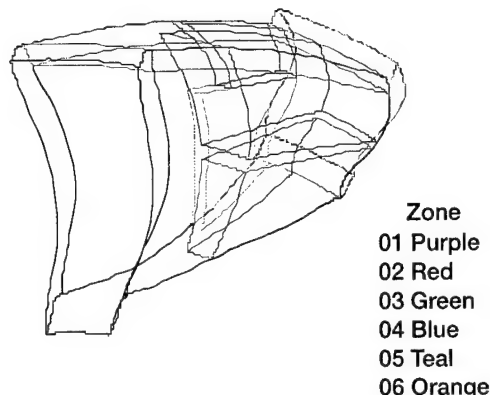
Zone 01: Casing endwall region—focus on clearance leakage and shock-endwall boundary-layer interactions

Zone 02: Casing endwall region, low-momentum region, including shock interaction effects—focus on pressure surface

Zone 03: Hub endwall region, low-momentum region—focus on pressure surface

Zone 04: Suction-surface, low-momentum region encompassing passage shock-boundary-layer interaction—focus on endwall region

Zone 05: Suction-surface, low-momentum region encompassing shock-boundary-layer interaction—focus on core flow region

Zone 06: Downstream region, mixing losses

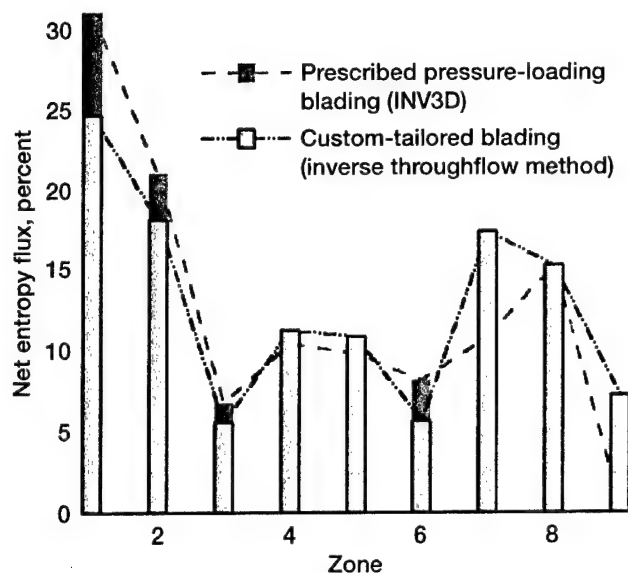Zone 07: Outer region, passage shock—focus on suction side

Figure 36.—Relative distribution of entropy production for rotor 1.

Zone 08: Outer region, passage shock—focus on pressure side

Zone 09: Inner region, passage shock—focus on core

The loss audit results are given in figure 36, where the entropy production from each zone is indicated in terms of its relative contribution to the overall entropy production. Also shown for comparison is a similar loss audit for the initial R1 designed using an inverse throughflow method. As expected, the endwall zone 01 has the largest loss contribution with approximately 30 percent of the total. Zone 02 accounts for a significant 20 percent of the total losses by capturing the transport of low-momentum fluid and its interaction with the passage shock near the pressure surface. The processes within these two endwall zones account for a little over 50 percent of the overall losses. A significant 44 percent of the total loss is attributed to the suction-surface viscous dissipation within zones 04 and 05 and the combined outboard shock loss from zones 07 and 08. The downstream mixing losses are on the order of 1 percent of the total but do not cover full mixing of the downstream flow field. Note that relative to the inverse throughflow design, the prescribed pressure-loading design has significantly lower shock and shock-boundary-layer-related losses.

Further information about the entropy production mechanisms in the casing endwall region (zone 01, 15-percent immersion from the casing) was gained by subdividing this region into seven smaller zones encom-
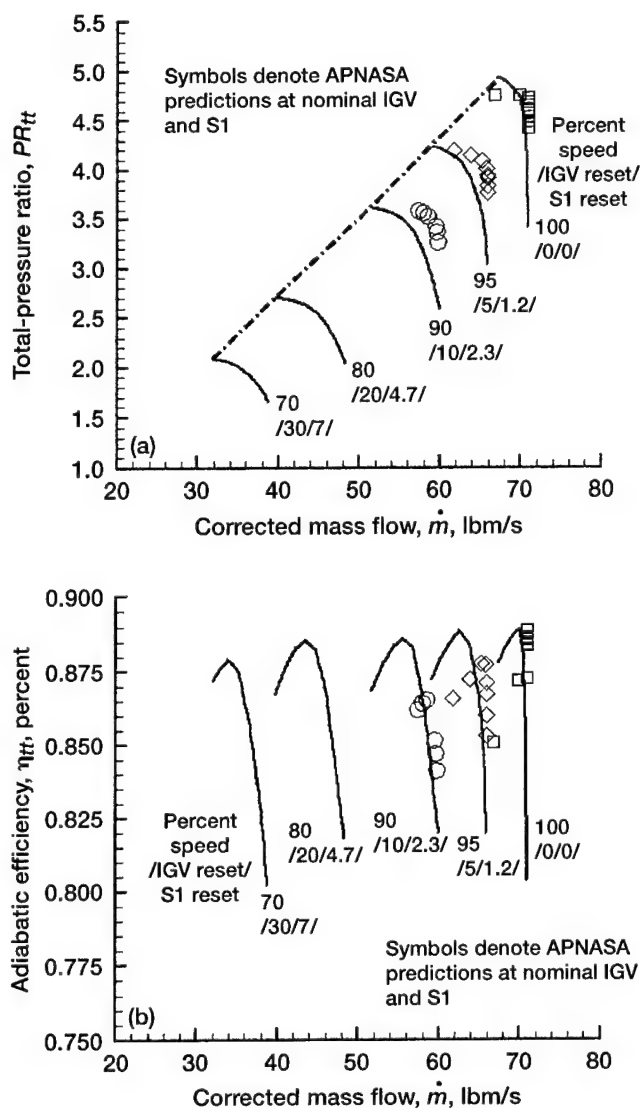

Figure 37.—Predicted overall performance characteristics. (a) Total-pressure ratio. (b) Adiabatic efficiency.

passing flow features thought to be critical and then performing a loss audit for the region. This audit indicated that tip clearance leakage and viscous dissipation along the endwall suction-surface corner contribute to approximately 40 percent of the total casing endwall entropy production. The passage shock and its interaction with the viscous endwall flow under the influence of the leakage vortex accounts for about 30 percent of the endwall entropy production. Although the spanwise transport of low-momentum fluid feeding the cesspool near the pressure surface corner directly contributes a relatively small amount to the endwall entropy production, its indirect impact on performance is linked to the downstream

24

mixing loss and the increased aerodynamic blockage. Thus, with this audit, various redesign strategies can be conceived and tested via numerical simulation to assess their relative benefits.

APNASA was used to simulate the off-design performance of the two-stage configuration at 100-, 95-, and 90-percent rotational speeds with nominal IGV and vane settings. The geometry was frozen as designed without accounting for structural deformation effects with varying operating conditions. The results of the simulation were used to construct stage characteristics for each of the two stages and these were subsequently stacked to predict the overall performance characteristics with various IGV and vane resets. The overall adiabatic efficiency predicted by APNASA was degraded by 1.46 percent, based on engineering judgment reflective of hardware quality shortfalls and other "X-factors" that may compromise the CFD predictive capability. Figure 37 shows the overall characteristics (total-pressure ratio and adiabatic efficiency) derived from the stage-stacking procedure at the indicated resets and compares them with APNASA predictions. Since there is no definitive application for this two-stage group, the adequacy of the characteristic map cannot be absolutely assessed. Nevertheless, a potentially adequate operating range seems to be available for further aerodynamic development.

Conclusions

In part I, very aggressive performance goals were defined by a rational perturbation of basic aerodynamic technology elements of current design systems. A potential for a substantial expansion of the aerodynamic design and operability space was shown. The research at NASA Glenn on practical means to effect these aerodynamic advancements is, in reality, still in its infancy. The challenge of discovering and developing new technology in a multistage turbocompressor environment requires a well-conceived plan of attack. Nevertheless, achievement of these advancements would give the design engineer the freedom to innovate.

A preliminary design of a four-stage compressor configuration was established for advanced technology development. This design was biased toward high efficiency at high loading. Three-dimensional blading and spanwise tailoring of vector diagrams were employed under the guidance of computational fluid dynamics (CFD) to control the aerodynamics of the high-loaded endwall regions. The preliminary results were encouraging and the front two stages were extracted for further aerodynamic trimming using a three-dimensional inverse design method.

In part II, the design principles for constructing blade-surface, pressure-loading distributions to be applied in a three-dimensional inverse design method were presented. This method produced blading having a high-efficiency potential relative to current practice. In addition, the inverse-designed blades were successfully adapted to the multistage environment using the APNASA code. An overall efficiency potential far exceeding current practice was demonstrated with the APNASA CFD.

In spite of the significantly higher aerodynamic loadings, advanced CFD-based tools were able to effectively guide the design of a very efficient two-stage compressor under state-of-the-art aeromechanical constraints. Adequate operability for aerodynamic research and development was predicted. This two-stage configuration can be used for further aerodynamic technology research and development to meet the goals established in part I.

Appendix A
Geometry

TABLE IV.—FLOW-PATH COORDINATES: DESIGN AERODYNAMIC INTENT

| Hub		Casing		Hub		Casing	
z, in.	r, in.	z, in.	r, in.	z, in.	r, in.	z, in.	r, in.
−10.000	4.993	−10.00	10.540	8.439	8.958	8.071	10.540
−9.000	4.993	−9.000	10.540	8.628	8.987	8.347	10.540
−8.000	4.993	−8.000	10.540	8.919	9.021	8.695	10.540
−7.044	4.993	−7.017	10.540	9.211	9.039	9.043	10.540
−6.090	4.993	−6.040	10.540	9.504	9.051	9.392	10.540
−5.136	4.993	−5.082	10.540	9.796	9.064	9.740	10.540
−4.181	4.993	−4.169	10.540	10.088	9.085	10.088	10.540
−3.225	4.993	−3.262	10.540	10.224	9.099	10.250	10.521
−2.717	5.015	−2.766	10.540	10.356	9.116	10.408	10.497
−2.417	5.039	−2.400	10.540	10.546	9.145	10.579	10.470
−2.118	5.071	−2.031	10.540	10.736	9.177	10.749	10.439
−1.820	5.112	−1.660	10.540	10.927	9.206	10.919	10.406
−1.523	5.162	−1.287	10.540	11.118	9.224	11.089	10.371
−1.228	5.221	−.913	10.540	11.311	9.221	11.258	10.334
−.605	5.377	−.412	10.540	11.604	9.182	11.604	10.253
.000	5.569	.000	10.540	11.815	9.133	11.813	10.202
.734	5.886	.518	10.540	12.023	9.071	12.021	10.149
1.420	6.294	1.039	10.540	12.229	9.004	12.230	10.096
2.094	6.721	1.559	10.540	12.437	8.940	12.439	10.043
2.777	7.134	2.080	10.540	12.647	8.886	12.647	9.991
3.489	7.495	2.601	10.540	12.842	8.850	12.887	9.932
3.869	7.645	3.072	10.540	12.981	8.834	13.008	9.903
4.258	7.766	3.551	10.540	13.120	8.826	13.129	9.875
4.677	7.873	4.052	10.540	13.259	8.824	13.251	9.848
5.100	7.964	4.553	10.540	13.399	8.822	13.372	9.822
5.524	8.052	5.054	10.540	13.538	8.819	13.494	9.797
5.947	8.146	5.555	10.540	13.785	8.806	13.786	9.741
6.367	8.252	6.057	10.540	13.979	8.790	13.978	9.707
6.561	8.310	6.359	10.540	14.172	8.771	14.170	9.678
6.754	8.374	6.662	10.540	14.365	8.749	14.363	9.651
7.052	8.485	6.889	10.540	14.557	8.727	14.557	9.629
7.347	8.603	7.116	10.540	14.751	8.713	14.751	9.610
7.642	8.719	7.342	10.540	14.962	8.710	14.962	9.594
7.940	8.828	7.569	10.540	15.466	8.709	15.466	9.575
8.245	8.918	7.796	10.540	15.970	8.709	15.970	9.575
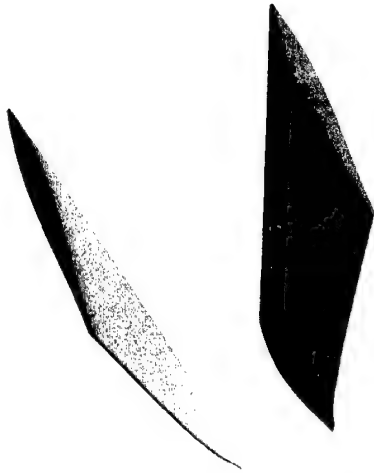
Figure 38.—Inlet guide vane, aft looking forward. Aspect ratio, 3.150; number of blades, 32.
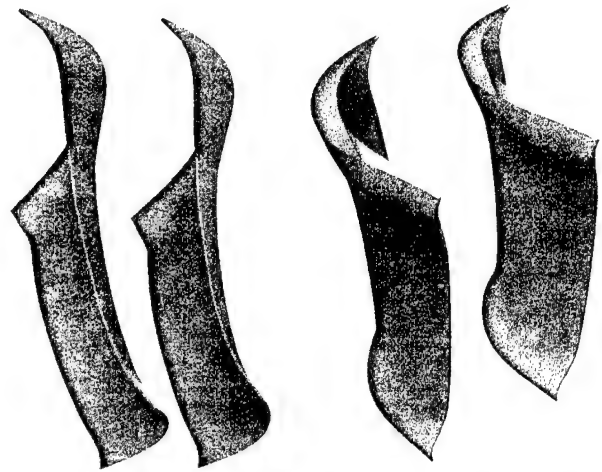

Figure 40.—Stator 1. Aspect ratio, 1.128; number of blades, 54.

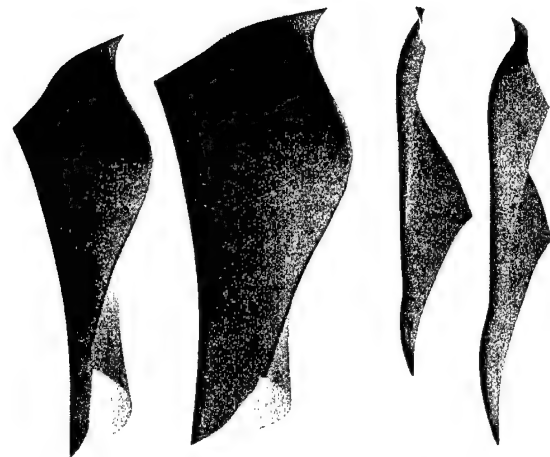Figure 39.—Rotor 1. Aspect ratio, 0.837; number of blades, 26.

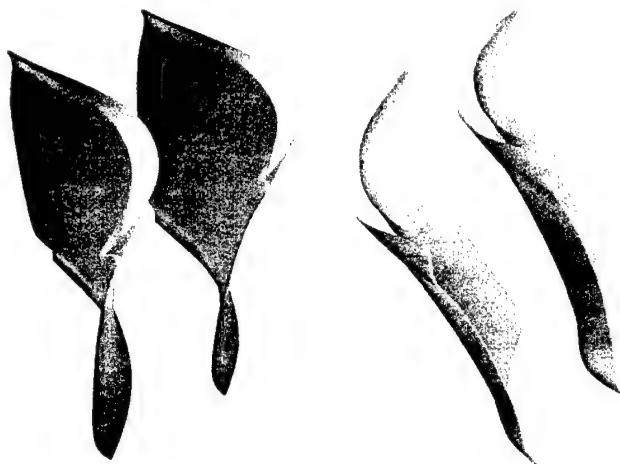Figure 41.—Rotor 2. Aspect ratio, 0.888; number of blades, 56.

Figure 42.—Stator 2. Aspect ratio, 0.923; number of blades, 74.
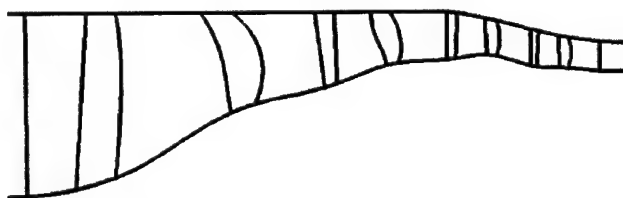

Figure 43.—Four-stage flow path with first two stages extracted for further aerodynamic development.

Appendix B
Computed Axisymmetric Averaged Spanwise Profiles at Design Throttle
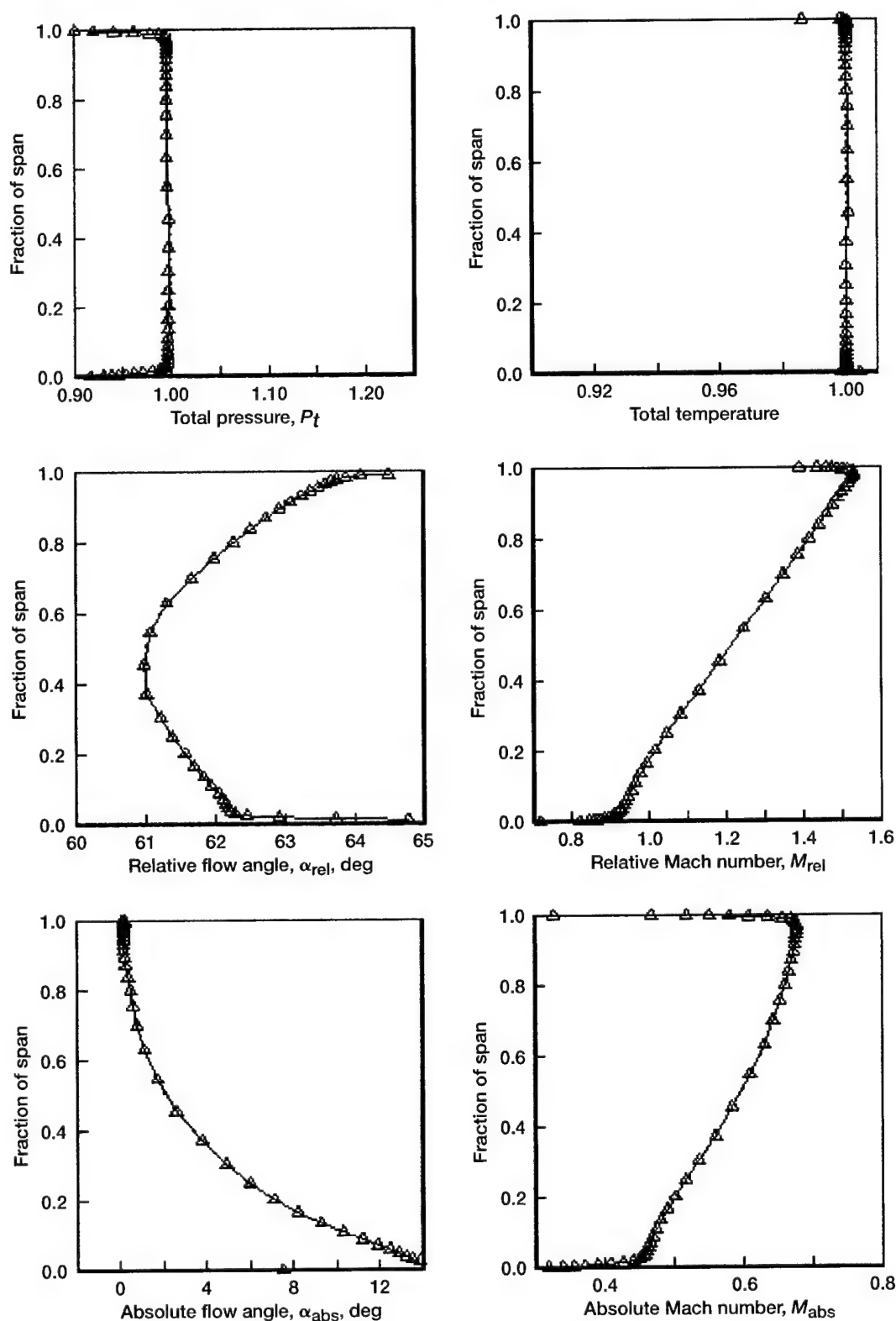
Figure 44.—Rectifying plane of inlet guide vane exit and rotor 1 inlet.
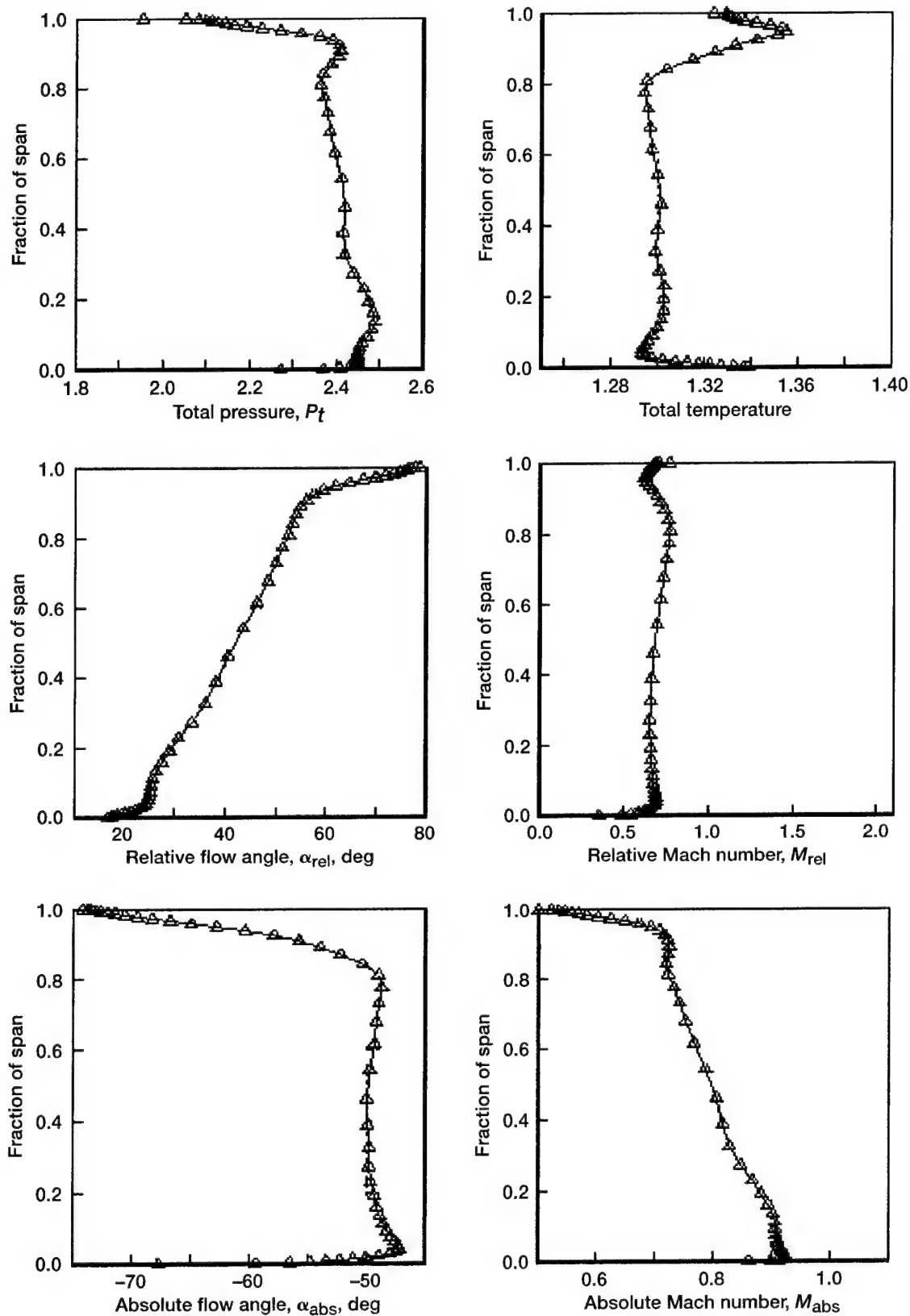
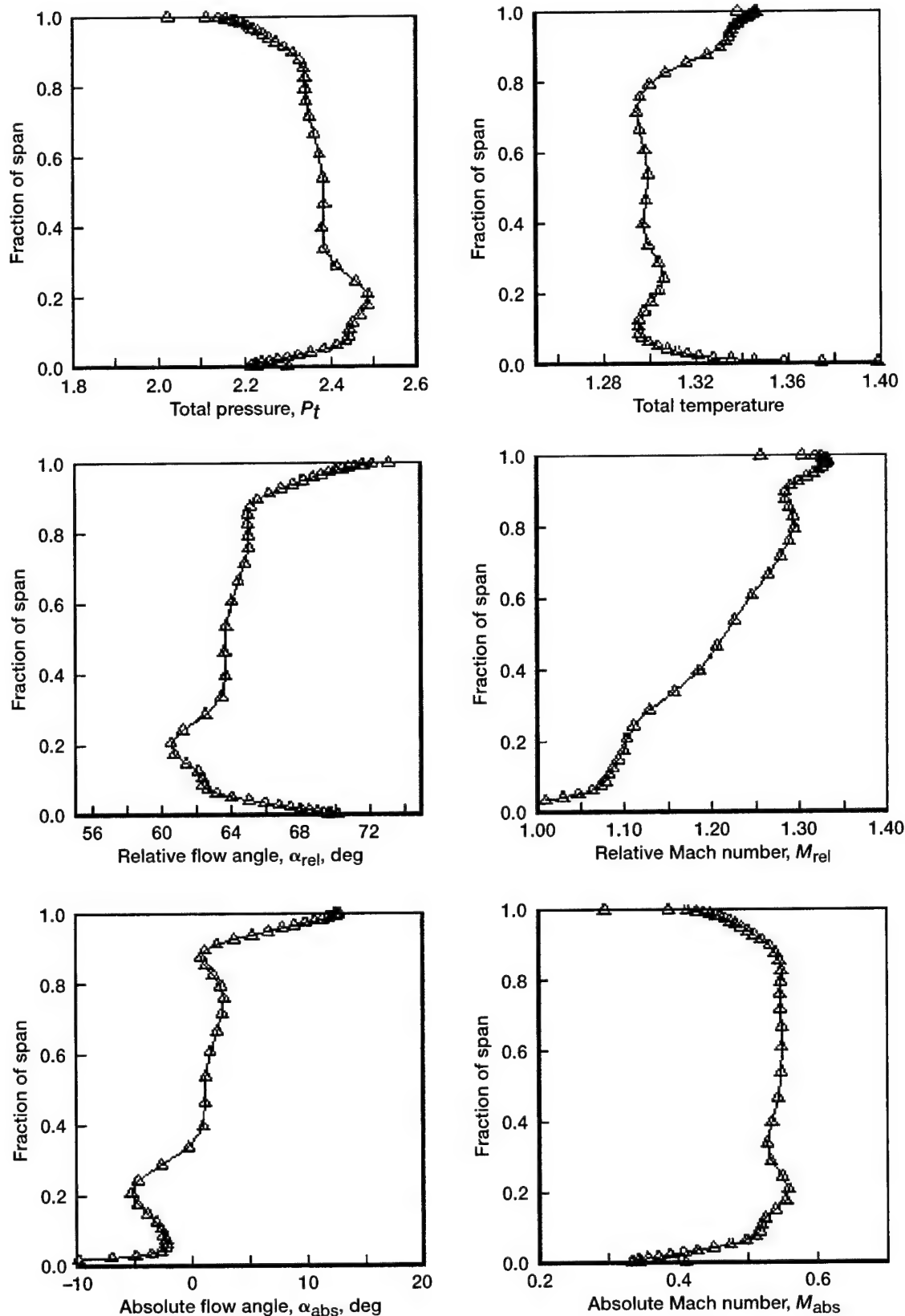Figure 45.—Rectifying plane of rotor 1 exit and stator 1 inlet.

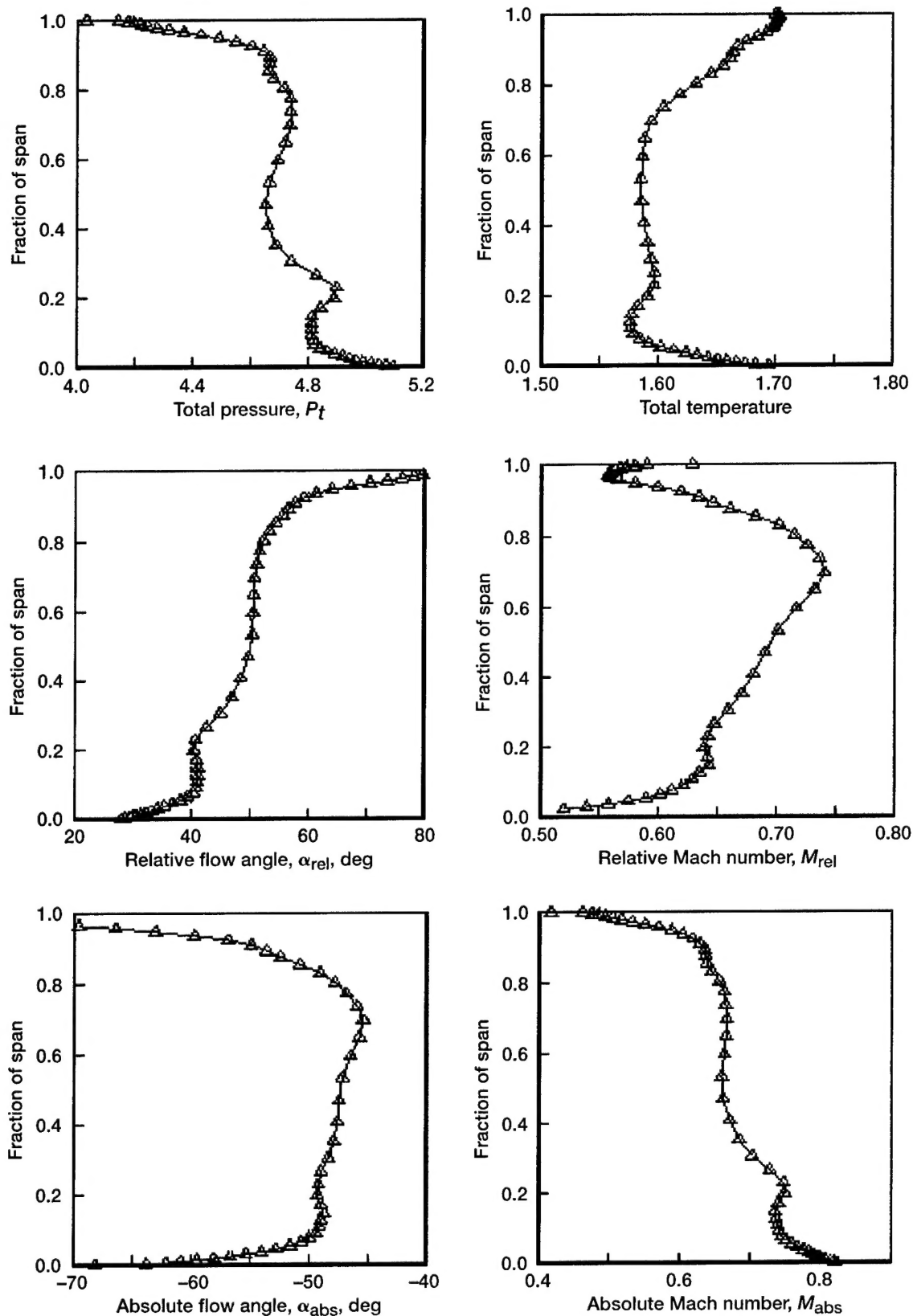Figure 46.—Rectifying plane of stator 1 exit and rotor 2 inlet.

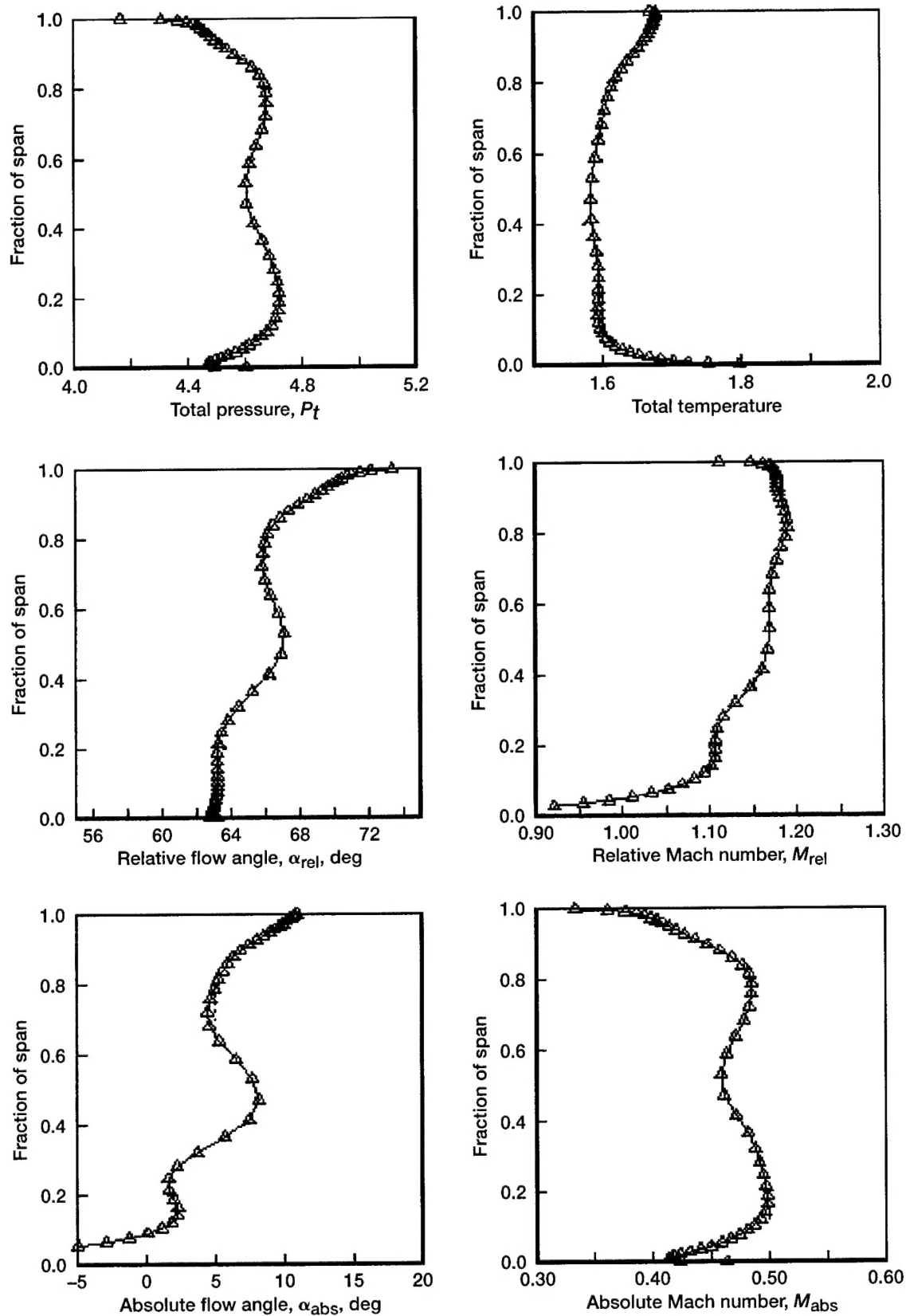Figure 47.—Rectifying plane of rotor 2 exit and stator 2 inlet.

Figure 48.—Rectifying plane of stator 2 exit.

References

1. Singh, Riti: Fifty Years of Civil Aero Gas Turbines. Aircraft Engineering and Aerospace Technology, vol. 68, no. 4, 1996, pp. 3–19.
2. Kerrebrock, J.L., et al.: Aspirated Compressors. ASME Paper 97–GT–525, 1997.
3. Kerrebrock, Jack L., et al.: A Family of Designs for Aspirated Compressors. ASME Paper 98–FT–196, 1998.
4. Dang, T.Q.: A Fully Three-Dimensional Inverse Method for Turbomachinery Blading in Transonic Flows. Trans. ASME J. Turbomachinery, vol. 115, no. 2, 1993, pp. 354–361.
5. Adamczyk, John J.: Aerodynamic Analysis of Multistage Turbomachinery Flows in Support of Aerodynamic Design. Trans. ASME J. Turbomachinery, vol. 122, no. 2, 2000, pp. 189–217.
6. Denton, J.D.: Loss Mechanisms in Turbomachines. Trans. ASME J. Turbomachinery, vol. 115, no. 4, 1993.
7. Greitzer, E.M.: REVIEW—Axial Compressor Stall Phenomena. Trans. ASME J. Fluids Eng., vol. 102, 1980, pp. 134–151.
8. Adkins, G.G., Jr.; and Smith, L.H., Jr.: Spanwise Mixing in Axial-Flow Turbomachines. Trans. ASME J. Engng. Power, vol. 104, 1982, pp. 97–110.
9. Koch, C.C.; and Smith, L.H., Jr.: Loss Sources and Magnitudes in Axial-Flow Compressors. Trans. ASME J. Engng. Power, vol. 98, 1976, pp. 411–424.
10. Koch, C.C.: Stalling Pressure Rise Capability of Axial Flow Compressor Stages. ASME J. Engng. Power, vol. 103, 1981, pp. 645–656.
11. Dzung, Lang S., ed.: Proceedings of a Symposium on Flow Research on Blading. Elsevier Pub. Co., Amsterdam, 1970.
12. Carmody, R.H.; and Seren, G.: Single-Stage Experimental Evaluation of Boundary Layer Blowing Techniques for High Lift Stator Blades. NASA CR–54567, 1968.
13. Khalid, S.A., et al.: Endwall Blockage in Axial Compressors. Trans. ASME J. Turbomachinery, vol. 121, no. 3, 1999, pp. 499–509.
14. Lee, N.K.W.; and Greitzer, E.M.: Effects of Endwall Suction and Blowing on Compressor Stability Enhancement. Trans. ASME J. Turbomachinery, vol. 112, 1990, pp. 133–144.
15. Wisler, D.C.; Koch, C.C.; and Smith, L.H., Jr.: Preliminary Design Study of Advanced Multistage Axial Flow Core Compressors. NASA CR–135133, 1977.
16. Hearsay, R.M.: A Revised Computer Program for Axial Compressor Design. ARL–75–0001, vols. 1 and 2, 1975.
17. Chima, Rodrick V.: Explicit Multigrid Algorithm for Quasi-Three-Dimensional Viscous Flows in Turbomachinery. J. Propulsion, vol. 3, no. 5, 1987, pp. 397–405.
18. Hall, E.J.; Topp, D.A.; and Delaney, R.A.: Task 7—ADPAC User's Manual. NASA CR–195472, 1996.
19. Jameson, A.; Schmidt, Wolfgang; and Turkel, Eli: Numerical Solution of the Euler Equations by Finite Volume Methods Using Runge Kutta Time Stepping Schemes. AIAA Paper 81–1259, 1981.
20. Denton, J.D.: The Calculation of Three-Dimensional Viscous Flow Through Multistage Turbomachines. Trans. ASME J. Turbomachinery, vol. 114, no. 1, 1992, pp. 18–26.
21. Damle, Sachin: Fully Three-Dimensional and Viscous Inverse Method for Turbomachine Blade Design. Ph.D. Dissertation, Syracuse University, 1998.
22. Damle, S., et al.: Practical Use of Three-Dimensional Inverse Method for Compressor Blade Design. Trans. ASME J. Turbomachinery, vol. 121, no. 2, 1999, pp. 321–325.
23. Dang, T.; Damle, S.; and Qiu, X.: Euler-Based Inverse Method for Turbomachine Blades, Part 2: Three-Dimensional Flows. AIAA J., vol. 38, no. 11, 2000, pp. 2007–2013.
24. Adamczyk, J.J., et al.: Simulation of Three-Dimensional Viscous Flow Within a Multistage Turbine. Trans. ASME J. Turbomachinery, vol. 112, no. 3, 1990, pp. 370–376.
25. Stringham, G.D., et al.: Design and Development of a Nine Stage Axial Flow Compressor for Industrial Gas Turbines. ASME Paper 98–GT–140, 1998.
26. Wellborn, Steven R.; and Delaney, Robert A.: Redesign of a 12-Stage Axial-Flow Compressor Using Multistage CFD. ASME Paper 2001–GT–0351, 2001.
27. Reynolds, Bruce; Subramanian, Mani; and Vitt, Paul: UEET Loss Audit for Two Stage POC Compressor. Order Number C–72909–K, ASE Technologies Project Report 00–063, 2000.

REPORT DOCUMENTATION PAGE

1. AGENCY USE ONLY (Leave blank)	2. REPORT DATE December 2002	3. REPORT TYPE AND DATES COVERED Technical Paper

4. TITLE AND SUBTITLE

Aerodynamic Design Study of Advanced Multistage Axial Compressor

5. FUNDING NUMBERS

WBS–22–714–03–27
1L161102AF20

6. AUTHOR(S)

Louis M. Larosiliere, Jerry R. Wood, Michael D. Hathaway, Adam J. Medd, and Thong Q. Dang

7. PERFORMING ORGANIZATION NAME(S) AND ADDRESS(ES)

National Aeronautics and Space Administration
John H. Glenn Research Center at Lewis Field
Cleveland, Ohio 44135–3191

8. PERFORMING ORGANIZATION REPORT NUMBER

E–13352

9. SPONSORING/MONITORING AGENCY NAME(S) AND ADDRESS(ES)

National Aeronautics and Space Administration
Washington, DC 20546–0001
and
U.S. Army Research Laboratory
Adelphi, Maryland 20783–1145

10. SPONSORING/MONITORING AGENCY REPORT NUMBER

NASA TP—2002-211568
ARL–TR–2859

11. SUPPLEMENTARY NOTES

Louis M. Larosiliere and Michael D. Hathaway, U.S. Army Research Laboratory, NASA Glenn Research Center; Jerry R. Wood, NASA Glenn Research Center; and Adam J. Medd and Thong Q. Dang, Syracuse University, Syracuse, New York 13244. Responsible person, Louis M. Larosiliere, organization code 5810, 216–433–3403.

12a. DISTRIBUTION/AVAILABILITY STATEMENT

Unclassified - Unlimited
Subject Category: 07   Distribution: Standard

Available electronically at http://gltrs.grc.nasa.gov

This publication is available from the NASA Center for AeroSpace Information, 301–621–0390.

12b. DISTRIBUTION CODE

13. ABSTRACT (Maximum 200 words)

As a direct response to the need for further performance gains from current multistage axial compressors, an investigation of advanced aerodynamic design concepts that will lead to compact, high-efficiency, and wide-operability configurations is being pursued. Part I of this report describes the projected level of technical advancement relative to the state of the art and quantifies it in terms of basic aerodynamic technology elements of current design systems. A rational enhancement of these elements is shown to lead to a substantial expansion of the design and operability space. Aerodynamic design considerations for a four-stage core compressor intended to serve as a vehicle to develop, integrate, and demonstrate aerotechnology advancements are discussed. This design is biased toward high efficiency at high loading. Three-dimensional blading and spanwise tailoring of vector diagrams guided by computational fluid dynamics (CFD) are used to manage the aerodynamics of the high-loaded endwall regions. Certain deleterious flow features, such as leakage-vortex-dominated endwall flow and strong shock-boundary-layer interactions, were identified and targeted for improvement. However, the preliminary results were encouraging and the front two stages were extracted for further aerodynamic trimming using a three-dimensional inverse design method described in part II of this report. The benefits of the inverse design method are illustrated by developing an appropriate pressure-loading strategy for transonic blading and applying it to reblade the rotors in the front two stages of the four-stage configuration. Multistage CFD simulations based on the average passage formulation indicated an overall efficiency potential far exceeding current practice for the front two stages. Results of the CFD simulation at the aerodynamic design point are interrogated to identify areas requiring additional development. In spite of the significantly higher aerodynamic loadings, advanced CFD-based tools were able to effectively guide the design of a very efficient axial compressor under state-of-the-art aeromechanical constraints.

14. SUBJECT TERMS

Machines for compressing air or other fluids; Compressors

15. NUMBER OF PAGES
41

16. PRICE CODE

17. SECURITY CLASSIFICATION OF REPORT Unclassified	18. SECURITY CLASSIFICATION OF THIS PAGE Unclassified	19. SECURITY CLASSIFICATION OF ABSTRACT Unclassified	20. LIMITATION OF ABSTRACT